Istituto Nazionale di Oceanografia e di Geofisica Sperimentale (Trieste, ITALY)

PEGASOS Project

ESTIMATION OF THE MEDIAN, NEAR FAULT GROUND MOTION IN SWITZERLAND.

SCIENTIFIC REPORT N. 7

Enrico Priolo[(1)], Alessandro Vuan[(1)], Peter Klinc[(1)], and Giovanna Laurenzano[(2,1)]

[(1)] *Istituto Nazionale di Oceanografia e di Geofisica Sperimentale (Trieste) – Seismological Research Centre Department (Udine), Italy*

[(2)] *Dipartimento di Ingegneria Civile - Università degli Studi di Trieste*

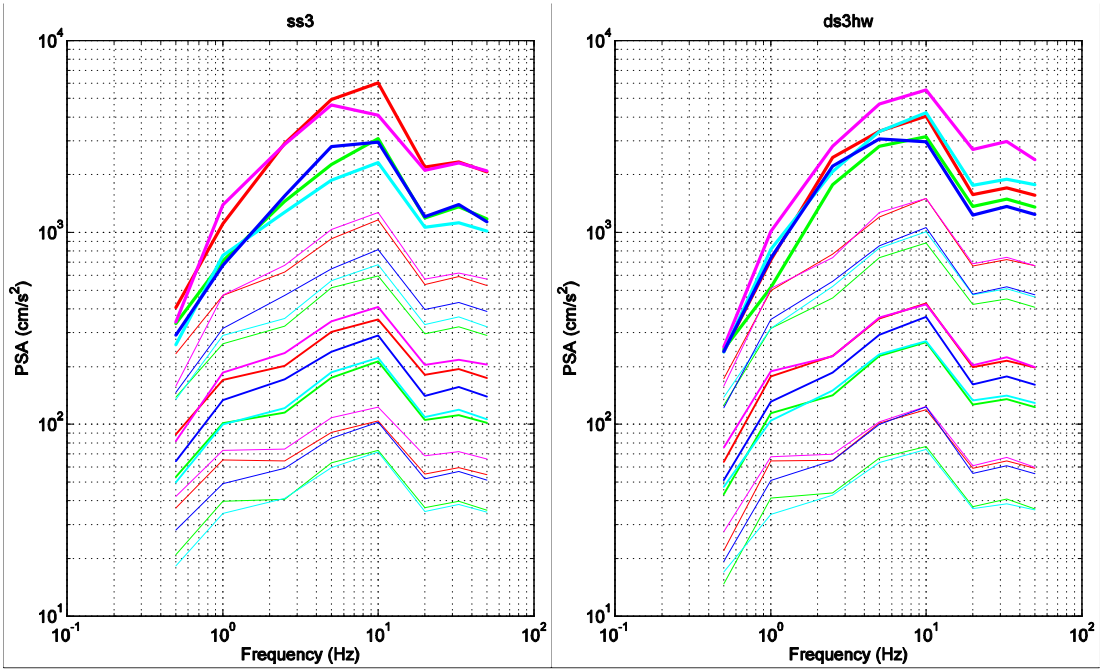

Scientific responsible: Dr. Enrico Priolo

Director of CRS Department: Dr. Enrico Priolo

Rel. OGS-32/2003/CRS-4
August 14th, 2003

Introduction

We perform some numerical simulations to assess the median ground motion for a $M = 6.5$ event at short distances from the fault. We take into account the 1-D Northern Switzerland model (CHN) and two fault mechanisms, i.e. vertical strike-slip and 45° dip-slip fault. In order to evaluate the ground motion variation with both distance and azimuth, seismograms are computed along five arrays of receivers at different distances from the fault ranging from 1 km to 25 km..

We focus on the median ground motion. For this reason, the source parametrization follows different criteria from those used in our previous study (Priolo et al., 2002), whose goal was to assess the maximum motion. Here, we define seismic moment (or slip) distributions having medium stress drop level and feature no sharp and localized asperities. Furthermore, instead of evaluating a single critical case, we need to build-up a robust statistics. Therefore, we take into account a large number of simulations for which we let to vary the slip distribution and rupture propagation (i.e., the aleatory parameters). Simulations are performed using EXWIM 2.1 method. Version 2.1 improves version 2.0, used in our previous study, in that it implements a hybrid low-frequency-deterministic, high-frequency-stochastic approach. The need of using a hybrid deterministic-stochastic approach comes from few observations (Liu and Helmberger, 1994) and a common acceptance among authors (for instance, Pitarka et al, 2000; Madariaga, 2002) of the fact that the signal looses its coherence in the high-frequency band (e.g., for $f > 2$ Hz) as an effect of the wavefield propagation through the earth. Any modelling method should take into account this aspect correctly (Madariaga, 2002). In particular, the high-frequency stochastic character of the seismogram is relevant when one wants to simulate realistic, highly likely situations. However, the use of a full deterministic approach (Priolo et al., 2002) is still justified to evaluate extreme cases in which the signal coherence persists in the high frequency band (Zahradnik, 2002b).

This report updates previous report n. 5 (Priolo et al., 2003a) with the results obtained using a more realistic set of slip distributions. See report n. 6 (Priolo et al., 2003b) for further details.

We first summarize the improvement of the new version of EXWIM, then we describe the setting of the numerical simulations, summarize the results obtained, and draw some conclusions.

EXWIM 2.1 Method

Version 2.1 of EXWIM improves the full deterministic approach of version 2.0 by introducing a stochastic hybridization of the signal in the high frequency band. The imple-

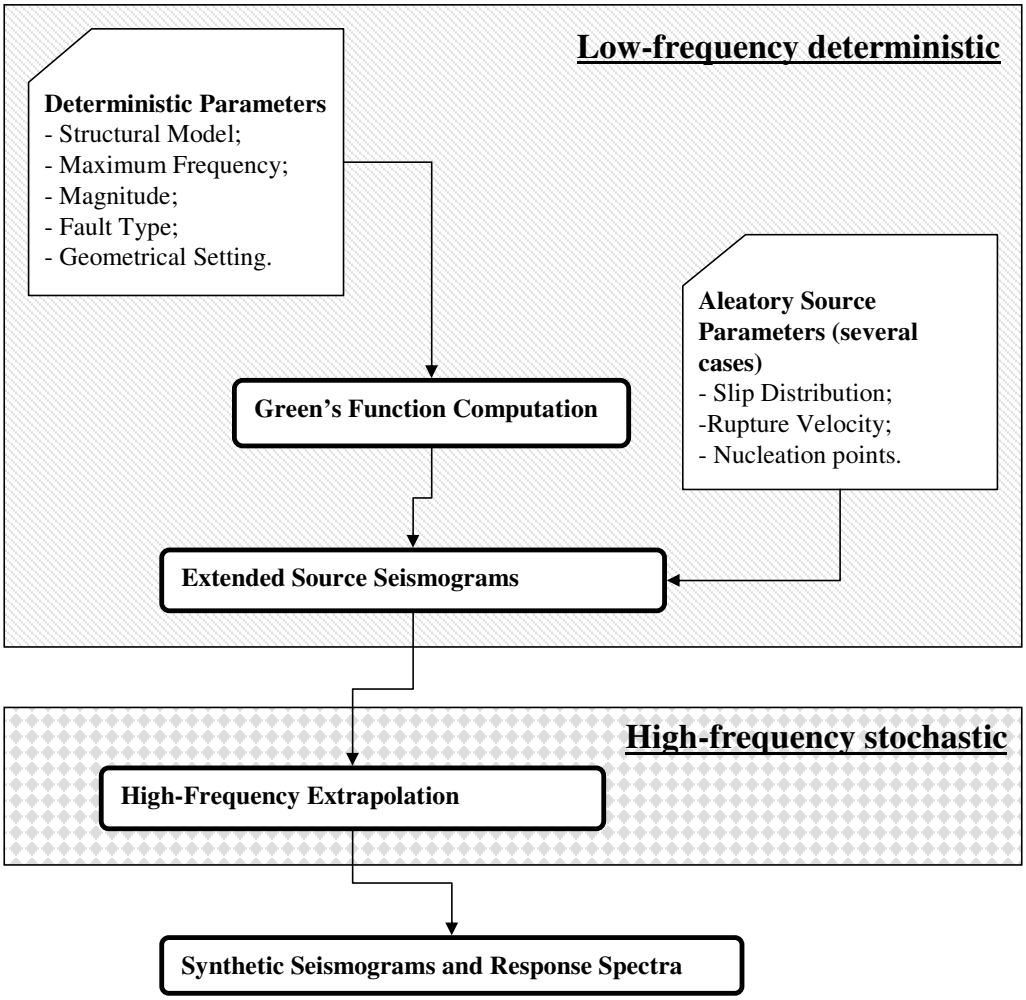

Figure 1: EXWIM 2.1 flow chart.

mentation of the stochastic approach is similar to the perturbation and extrapolation method (PEXT) recently introduced by Zahradnik and Tselentis (2001) and Zahradnik (2002a). We introduce some changes in order to preserve the deterministic spectrum of both amplitude and phase in the low frequency band, avoid the spectral holes displayed by most hybrid methods in the cross-over band, and take into account a high-frequency spectral decay according to a pre-assigned attenuation law.

A schematic description of EXWIM 2.1 is illustrated in Figure 1. At first, seismograms for rupture propagating along an extended fault are computed deterministically in the low-frequency band. The computational procedure of this part coincides with EXWIM 2.0, whose description can be found in (Priolo et al., 2002). In this study, rupture velocity is

NORTHERN SWITZERLAND (CHN)					
H (km)	α (km/s)	β (km/s)	ρ (t/m^3)	Q_α	Q_β
0.05	1.73	1.00	1.66	130	60
0.05	2.07	1.20	1.76	130	60
0.05	2.77	1.60	2.06	220	100
0.45	4.84	2.80	2.55	440	200
0.40	5.88	3.40	2.75	440	200
25.0	6.23	3.60	2.85	660	300
30.0	7.95	4.60	3.00	1100	500
HSP	7.95	4.40	3.00	1100	500

Table a: Structural model of Northern Switzerland (CHN). Model parameters are: H = layer thickness; (α, β) = P- and S-wave velocities; ρ = density; (Q_α, Q_β) = P- and S-wave quality factors. HSP means half-space continuation.

held constant to 0.8 V_S. The low-frequency deterministic signal includes all details of the wave propagation through the structural model, near-field terms, and focal mechanism. This signal defines a deterministic envelope, which is filled up by the high-frequency signal with random phase. The spectral amplitude of the high-frequency stochastic signal is set by the amplitude of the deterministic spectrum in its high frequency limit, and it is defined in two ways, that is by either setting a flat plateau or using a pre-defined frequency-dependent attenuation law. The transition between the deterministic and stochastic signal is made smooth by blending the deterministic and stochastic spectra within a cross-over band.

Description of the Simulations

Simulations are performed for the Northern Switzerland model (CHN, Table a) and for two fault mechanisms. The values of the parameters used for the two cases are described in Table b. The geometrical settings are illustrated in Figure 2.

For the low-frequency deterministic part, the maximum computational frequency of the Green's functions is set at $f_{max} = 2.5$ Hz, and the fault is discretized by a 51×101 grid of elementary sources, for all distances. The high-frequency stochastic contribution is added to each seismogram up to the maximum frequency of 20 Hz, which is therefore the maximum frequency of the final seismograms. The deterministic-to-stochastic cross-over band is set at [1 Hz, 2 Hz].

In the low-frequency band (i.e. $f < 2$ Hz), the fault rupture is described by a kinematic approach using a k^{-2} seismic moment density distribution (Herrero and Bernard, 1994). The slip duration is set at 0.5 s. A complete description of the source model is given in (Priolo et al., 2002). As requested by NAGRA, the average stress drop is set at a medium

	CASE 1 (SS)	CASE 2 (DS)
Structural model	CHN (Northern Switzerland)	
Mechanism	Strike-slip	Dip-slip
Dip	90°	45°
Magnitude	6.5	
Rupture dimension ($L \times W$)	25 km x 12.5 km	
Depth of fault top	1000 m	
Stress-drop ($\Delta\sigma$)	Median[(*)]	
	1.5 MPa	2.0 MPa
N. of slip-distributions	5	
Rupture-velocity	0.8 Vs	
N. of nucleations	153 (for each slip distribution)	
N. of sites (for each distance)	11, located along rupture (one half of fault)	20, located in "race track ", hanging wall and foot wall
Site distances	1 km, 3 km, 5 km, 10 km, 25 km	
Total n. of sites	55	100
Max. computational frequency (f_{max})	20 Hz	
Deterministic-stochastic transition band	[1 Hz, 2 Hz]	

(*) See also table 2d in (Priolo et al., 2002).

Table b: Description of the simulated cases

level (Priolo et al., 2002), thus the size of the fault is sat at an average value.

To estimate the median ground motion, we need to take into account the uncertainty due to the aleatory parameters (i.e., slip distribution and rupture starting point) and perform a statistics on a large number of simulations. We consider 5 different slip k^{-2}-distributions and 153 nucleation points (Figures 3 and 4), for a total population of 765 rupture scenarios. Thus, at each of the 155 sites we compute 765 three-component seismograms for each of the two fault mechanisms. The amount of the final data-set is summarized in Table c.

The five slip distributions used here were introduced in previous report n. 6 (Priolo et al., 2003b) to correct two features of the distributions defined in report n. 5 (Priolo et al., 2003a), that were considered unrealistic: 1) the slip was distributed over a large part of the fault and featured rather regular and sharp boundaries, with the effect of increasing the low frequency amplitude; and, 2) large slip values were assigned to the shallow part of the fault.

The new distributions show large parts of null slip and incoherent slip boundaries. In addition, the slip is distributed mainly in the bottom half of the fault (i.e., at larger depths than the previous set). Thus we avoid unrealistic near surface ruptures.

Computations have been performed on the high performance parallel computers of the CINECA computing center (Bologna, Italy), and took about one week of an IBM SP4 computer with 64 dedicated processors.

	CASE 1 (SS)	CASE 2 (DS)	TOTAL
N. of sites	55	100	155
N. of Green's functions for each site	5151	5151	5,151
Total n. of Green's functions	283,305	515,000	798,405
N. of slip distributions	5	5	5
N. of nucleations	153	153	153
N. of seismograms for each site	765	765	1530
Total n. of seismograms	42,075	76,500	118,575

Table c: Summary of the computations performed in this study

Results

The results consist of three-component displacement waveforms and acceleration response spectra. Due to the huge amount of output data, a reduced data-set of PGA and spectral accelerations at the eight frequencies of 0.5, 1.0, 2.5, 5.0, 10, 20, 33, and 50 Hz is provided. The whole data-set (about 10 GB on disk), or part of it, is available on demand.

Figure 5 shows the mean horizontal PGA estimated at all sites from all simulations. The horizontal ground motion is the average of the two horizontal components. The experimental layout is that of Figure 2. The maps clearly show both radial and azimuthal variations of the ground motion. The two mechanisms provide comparable maximum values (i.e., about 2 m/s^2), but feature different distributions of the peaks with azimuth. In fact, in the strike-slip case the ground motion peak occurs near to half fault length at the shortest distance, and moves toward the fault tip direction as the site distance increases. On the other hand, for the dip-slip the lobe of the maximum values spread over a wide area located on the hanging wall obliquely to the fault tip. Obviously, this result depends on the particular fault geometry and position within the structural model that have been chosen for our simulations, on the slip distributions, as well as on the geometry of the sites. Note also that the values displayed in the maps have been obtained including all the possible rupture scenarios, and therefore they take into account all possible rupture directions, such as up-dip, down-dip, bilateral, and both forward and backward unilateral.

Figure 6 and 7 show the spectral pseudo-accelerations obtained for the two fault mechanisms, respectively. Both shape and steepness of the spectral curves obtained for the two mechanisms are comparable each other. The spectral decay toward the low frequencies is uniform, especially for the curves obtained considering the maximum values (thick lines). In contrast, some median curves (thin lines) still feature amplification at about 1 Hz, especially for the strike-slip case. The variability of the values resulting from the different slip distributions is within a factor three, the largest values being obtained for those distributions featuring a large asperity (i.e., n. 1 and 3).

The lower values obtained for the dip-slip case are explained by the fact that the geometry of the receivers includes locations corresponding to low directivity, i.e. on the

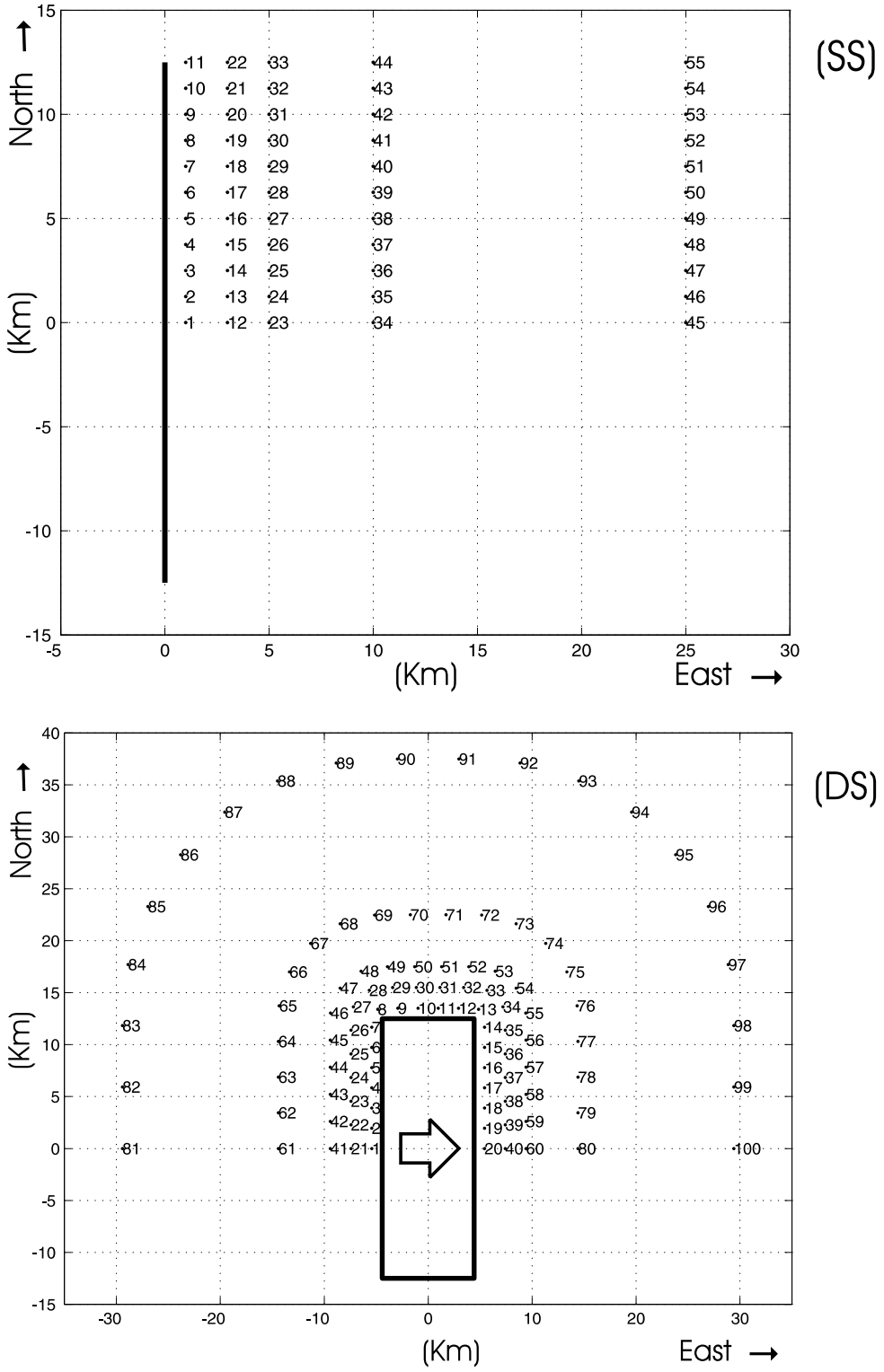

Figure 2: Geometrical settings (top view) defined for the simulations: (SS) Strike-slip; (DS) dip-slip. Solid lines defines the fault area projection on the surface. The arrow shows down-dip direction. The numbers indicate the site locations.

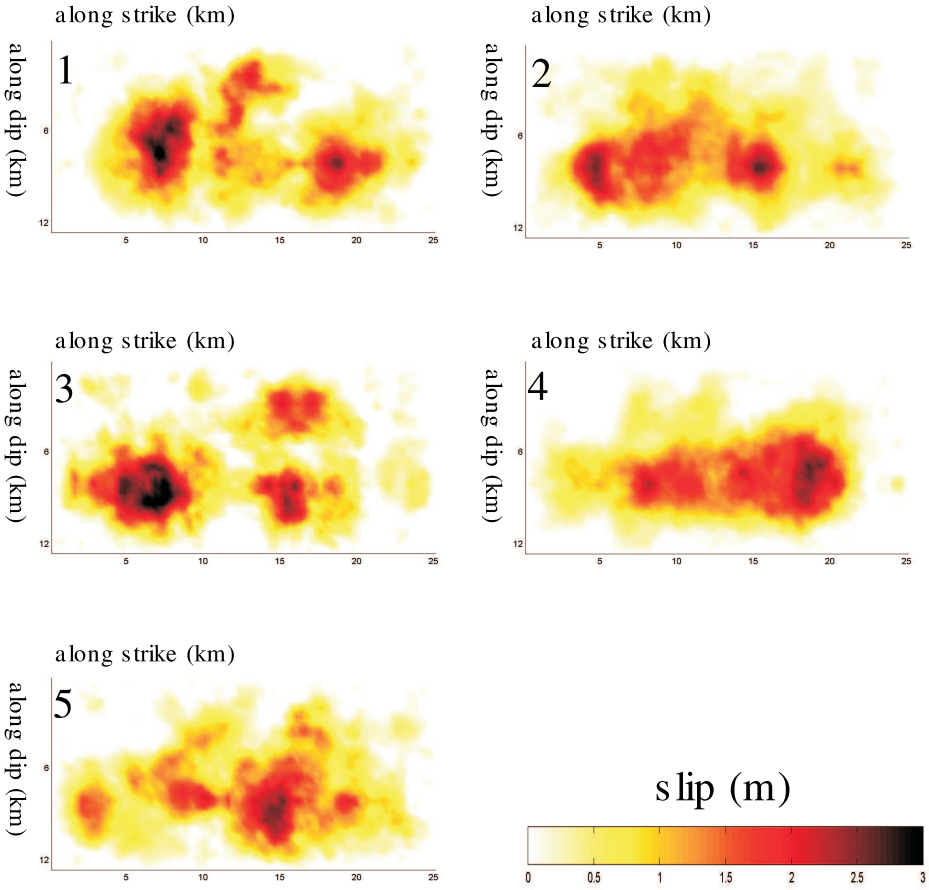

Figure 3: The five different k^{-2} seismic moment distributions (Herrero and Bernard, 1994) used in the simulations.

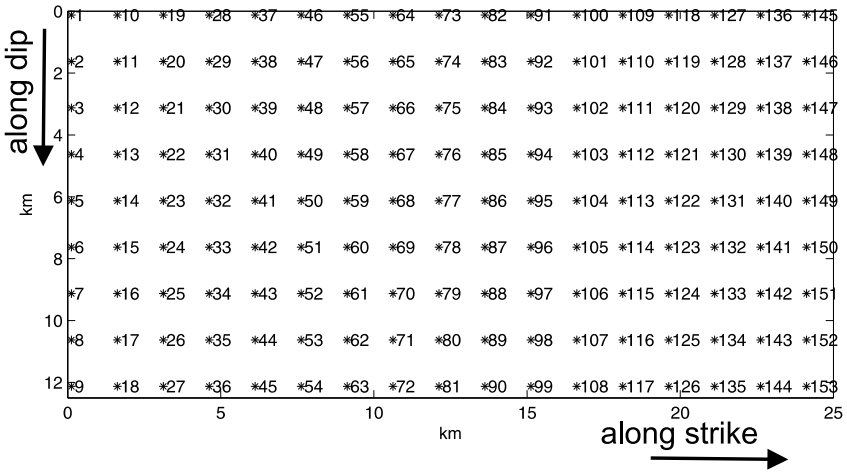

Figure 4: Location of the nucleations on fault.

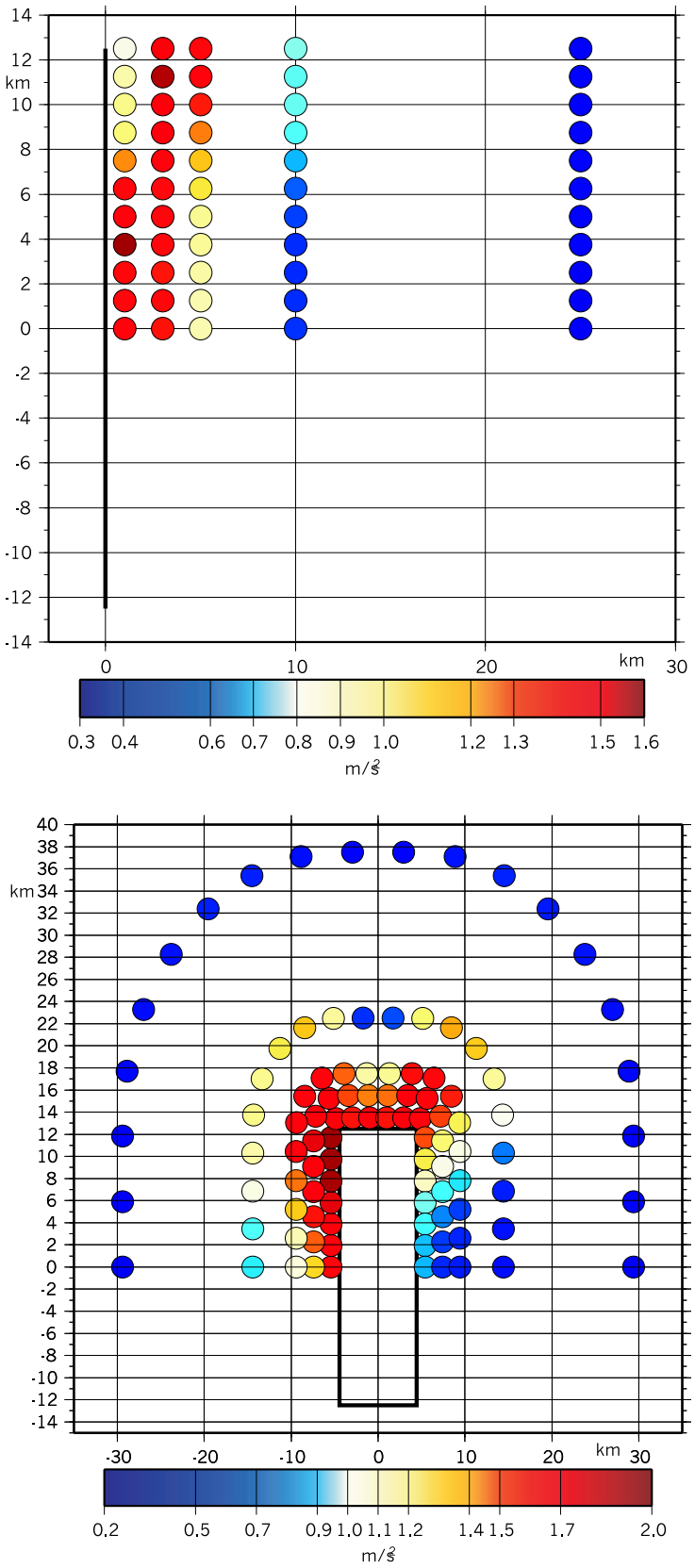

Figure 5: Peak ground acceleration (mean value) estimated at all sites. Top panel: strike-slip; bottom panel: dip-slip. The thick black line indicate the fault projection on earth's surface.

footing wall of the fault. In fact, the values obtained considering only the receivers located on the hanging wall (Figure 8) are completely comparable to those obtained for the strike-slip.

Figures 9-12 and 18-21 show the acceleration waveforms (horizontal components) computed for the strike-slip and dip-slip mechanisms, respectively, and for seismic moment distribution n. 1. Two different rupture directions are shown, i.e. an up-dip, forward unilateral rupture and an up-dip bilateral rupture (nucleation points n. 26 and 80 of Figure 4, respectively).

Figures 13-17 and 22-26 show PGA and spectral accelerations (mean value and mean value plus/minus the first standard deviation) estimated for the eight reference periods for the strike-slip and dip-slip mechanisms, respectively. The maximum spectral acceleration occurs at periods from 0.1 s to 0.2 s, in all cases. It is worth noting that, with dip-slip mechanism, the strike direction represents a point of local minimum of the spectral accelerations.

With the exception of the two longest periods of 1 s and 2 s, the statistical upper bound (mean plus the first standard deviation) of the spectral acceleration of this study compare well to those estimated for the upper limit ground motion (Priolo et al., 2002), in the sense that they are in general considerably lower. The inconsistency found at the two longest periods is due to the choice of the seismic moment distribution made in (Priolo et al., 2002) — one dominant and localized asperity —, which had the effect of dropping the energy in the low frequency band. This fact was already outlined by the experts.

Finally, Figures 6 and 7 show a sample of the acceleration response spectra obtained for the SS and DS mechanisms, respectively. The spectra refer to seismic moment distribution n. 1 (i.e., 153 spectra) and three groups of sites aligned along three different azimuths. It can be appreciated both the variability of the ground motion as a function of the different ruptures as well as the directivity effect, which shows up with the spectral peak at about 1 Hz.

Conclusions

We have estimated the median strong ground motion in the near-fault range. Sites located at five Joyner and Boore distances have been considered. Simulations have been performed for two mechanisms typical of strike-slip and dip-slip, respectively. A robust statistics has been built-up by considering a large number of sites at different azimuths, five slip distributions and a large number of rupture nucleations from different points of the fault.

This report updates the results obtained in previous report n. 5 (Priolo et al., 2003a) by using a different set of slip distributions as an input for the simulations. These distributions are considered more realistic than the previous one, in that the whole fault segment

appears as a patch of a number of asperities and the main part of the rupture occurs in the deepest half of the fault. To our knowledge, they can ultimately be considered as realistic.

The computed pseudo-accelerations show rather regular low-frequency spectral decay. The two mechanisms produce similar acceleration values, though different spatial distributions of the ground motion.

Acknowledgements

The Wavenumber Integration Method is part of the package Computer Programs in Seismology developed by R. B. Herrmann at St. Louis University (Herrmann, 1996a; Herrmann, 1996b). The bulk of computations has been performed at the *Consorzio Interuniversitario del Nord Est Italiano per il Calcolo Automatico, Bologna, Italy* (CINECA), within an agreement existing between OGS and CINECA. We thank C. Calonaci of CINECA for his assistance. We thank A. Michelini for the revision of this report.

1 References

Herrero, A., and Bernard, P. (1994). A kinematic self-similar rupture process for earthquakes. *Bull. Seism. Soc. Am.*, **84**, 1216-1228.

Liu, H. L., and D. V. Helmberger (1985). The 23:19 aftershock of the 15 October 1979 Imperial Valley earthquake: more evidence for an asperity. *Bull. Seism. Soc. Am.*, **75**, 689-708.

Madariaga, R. (2002). Assessment of feasibility of kinematic fault models used for upper limit ground motion evaluations for the Pegasos project. Pegasos Project, Technical Note n. EXT-TN-0308, 8 pp.

Pitarka, A., Sommerville, P., Fukushima, Y., Uetake, T., and Irikura, K. (2000). Simulation of near-fault strong-ground motion using hybrid Green's functions. *Bull. Seism. Soc. Am.*, **88**, 54-68.

Priolo, E., Vuan, A., Klinc, P., and Laurenzano, G. (2002). *PEGASOS Project — Estimation of the ground motion upper limit in Switzerland: EXWIM numerical simulations. Scientific Report n. 4 - Revised Final Report.* Report n. OGS-48/2002/CRS-6. Borgo Grotta Gigante, November 28, 2002. 79 pp.

Priolo, E., Vuan, A., Klinc, P., and Laurenzano, G. (2003a). *PEGASOS Project — Estimation of the median, near fault ground motion in Switzerland. Scientific Report n. 5* Report n. OGS-21/2003/CRS-2. Borgo Grotta Gigante, June 10, 2003. 30 pp.

Priolo, E., Vuan, A., Klinc, P., and Laurenzano, G. (2003b). *PEGASOS Project — Estimation of the ground motion upper limit in Switzerland: EXWIM numerical simulations. Scientific Report n. 6* Report n. OGS-27/2003/CRS-3. Borgo Grotta Gigante, June 30, 2003. 7 pp.

Zaharadnik, J. (2002a). Numerical simulations of ground motions for finite sources by a deterministic-stochastic method PEXT. *PEGASOS SP2 Workshop 2, 16-18 April, 2002, Zurich (Switzerland).* CD-ROM.

Zahradnik, J. (2002b). Comments on the report by Pitarka et al., entitled "Numerical simulations for evaluation of median and upper limit ground motions in Switzerland" (including the comparison between the URS and OGS simulations). Written communication, December 5, 2002.

Zahradnik, J. and Tselentis (2002). *Modelling strong-motion accelerograms by PEXT method, aplication to the Athens 1999 earthquake.* http://seis30.karlov.mff.cuni.cz/papers/strong/

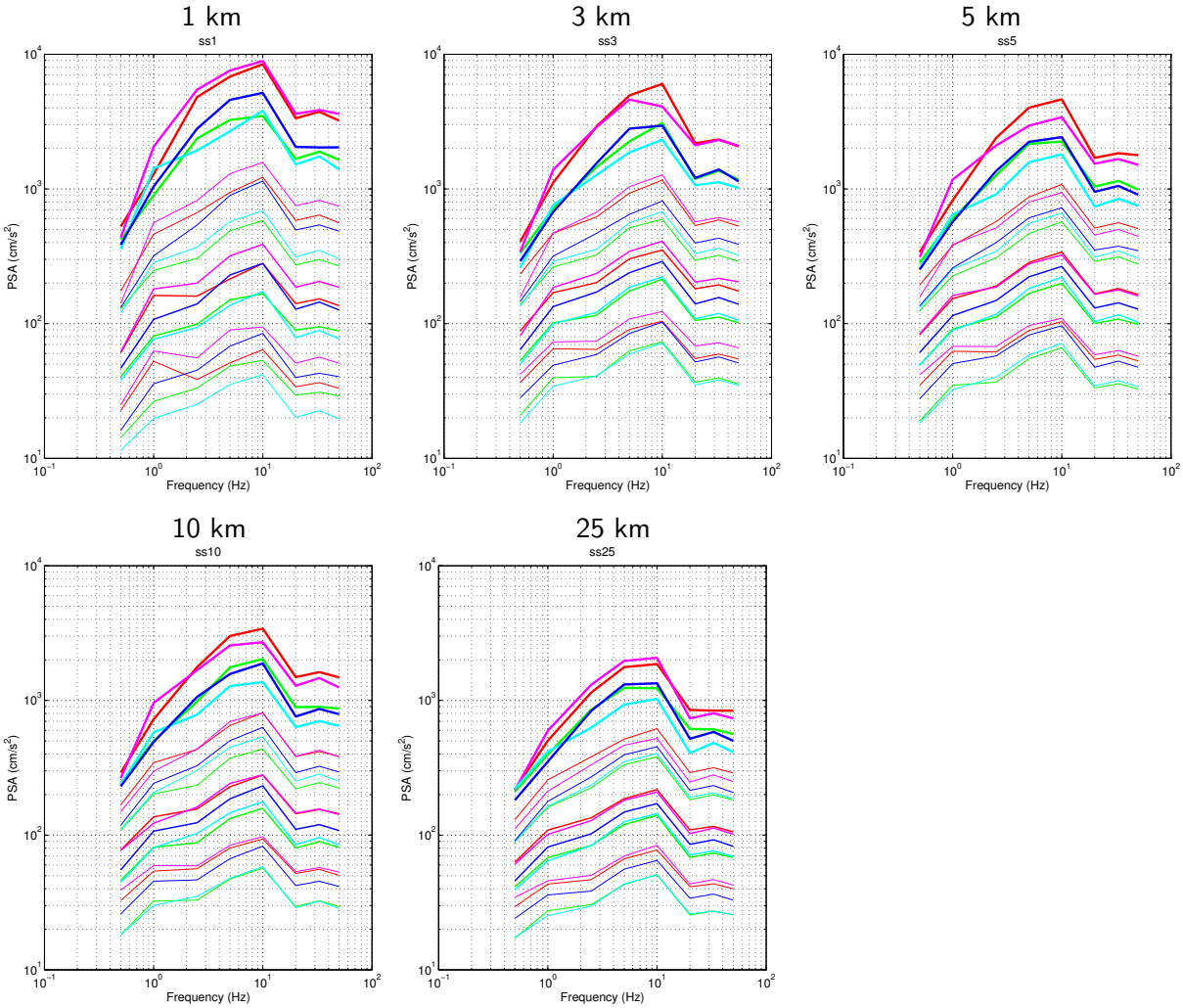

Figure 6: Case SS. Pseudo-acceleration computed at the five reference distances for the five slip distributions of Figure 3. Each color represents the results obtained for a single slip distribution (1: red; 2: green; 3: magenta; 4:cyan; 5: blue) The statistic is built up by considering for each slip distribution all receivers and nucleation points (see Figures 2 and 4, respectively). Thick lines: median of the maximum values. Thin lines: median of the median values and median plus/minus the first standard deviation (thinnest lines).

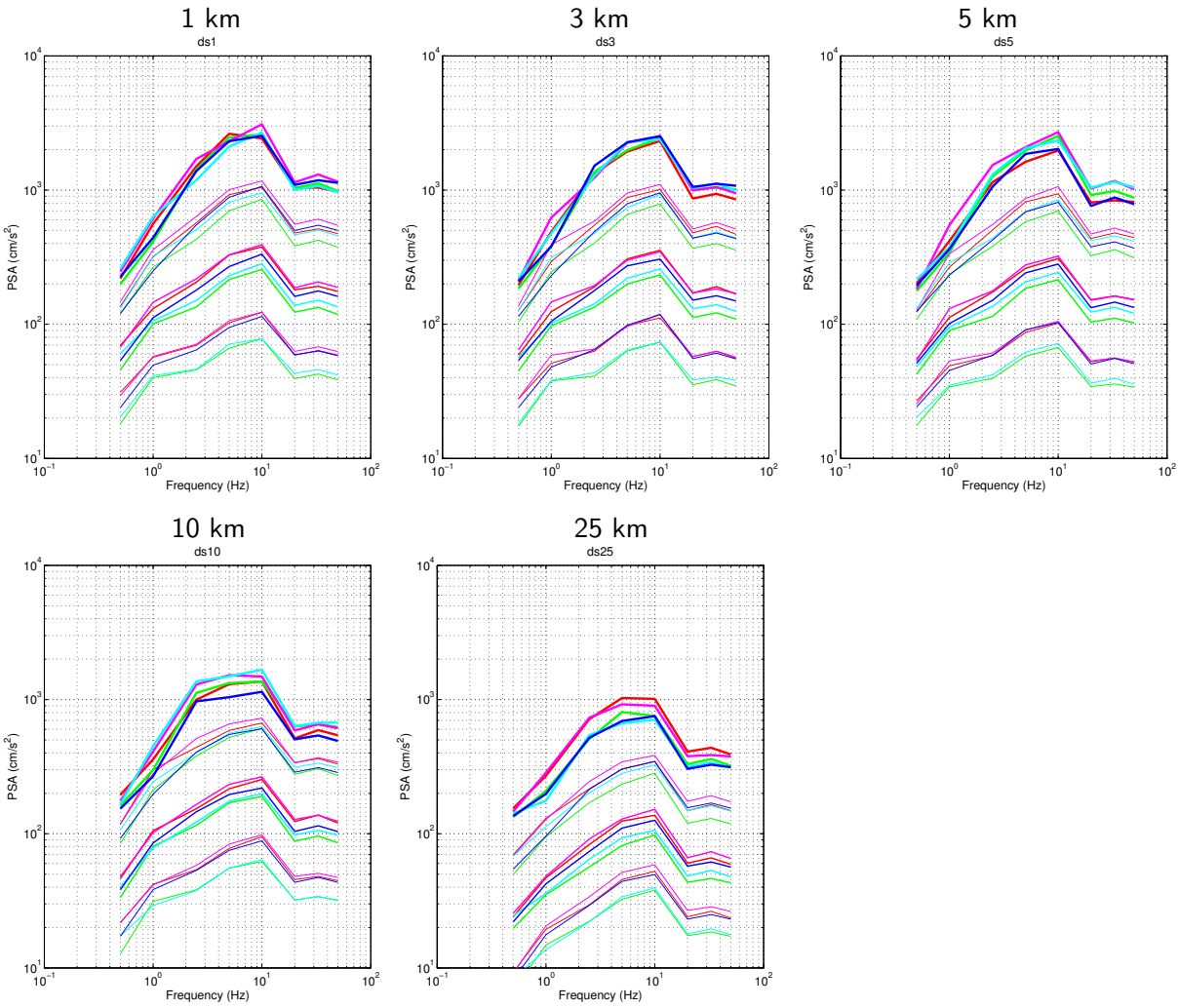

Figure 7: Same as Figure 6, but for case DS.

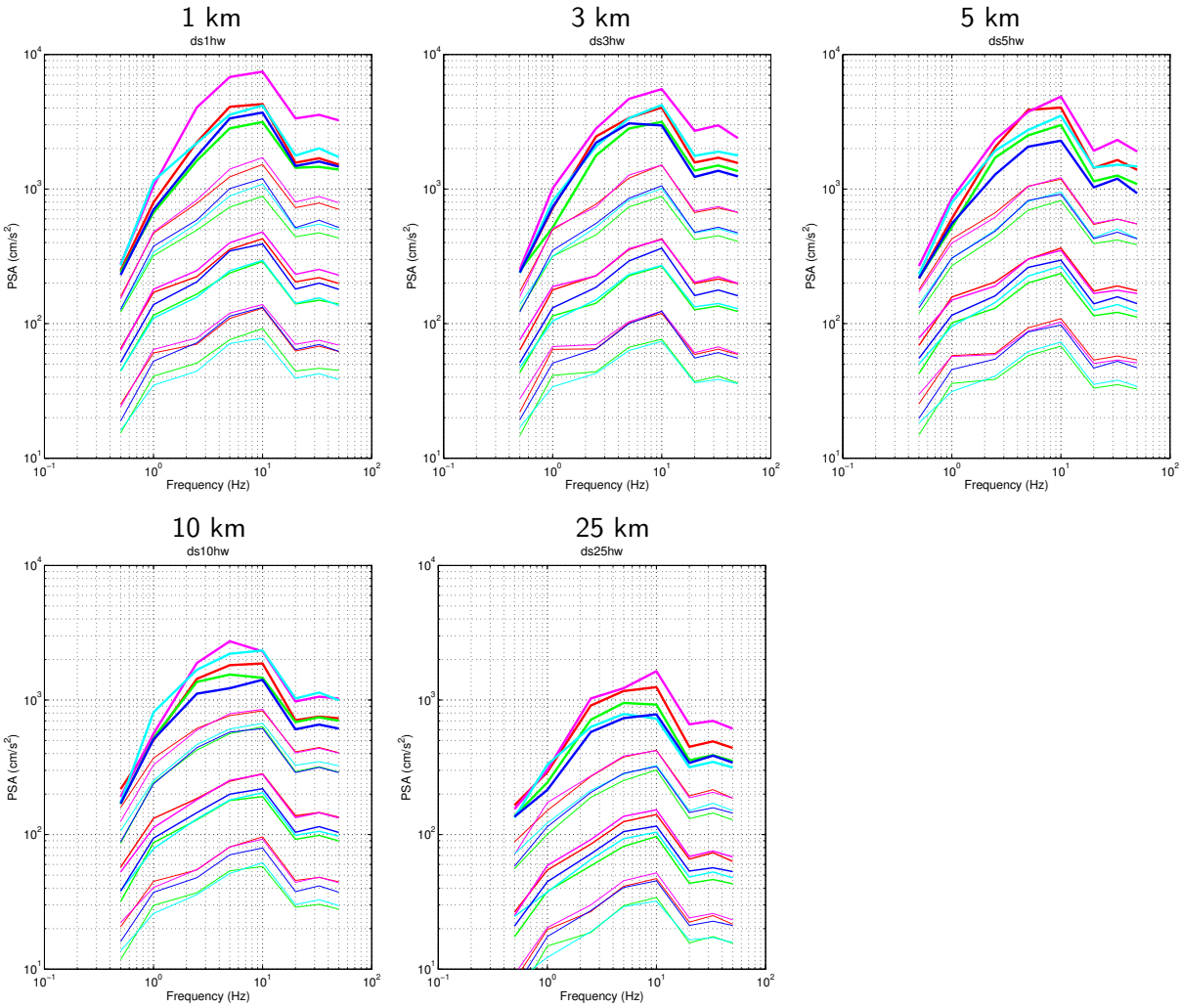

Figure 8: Same as Figure 7 (i.e., dip-slip mechanism), but considering only receivers located on the hanging wall.

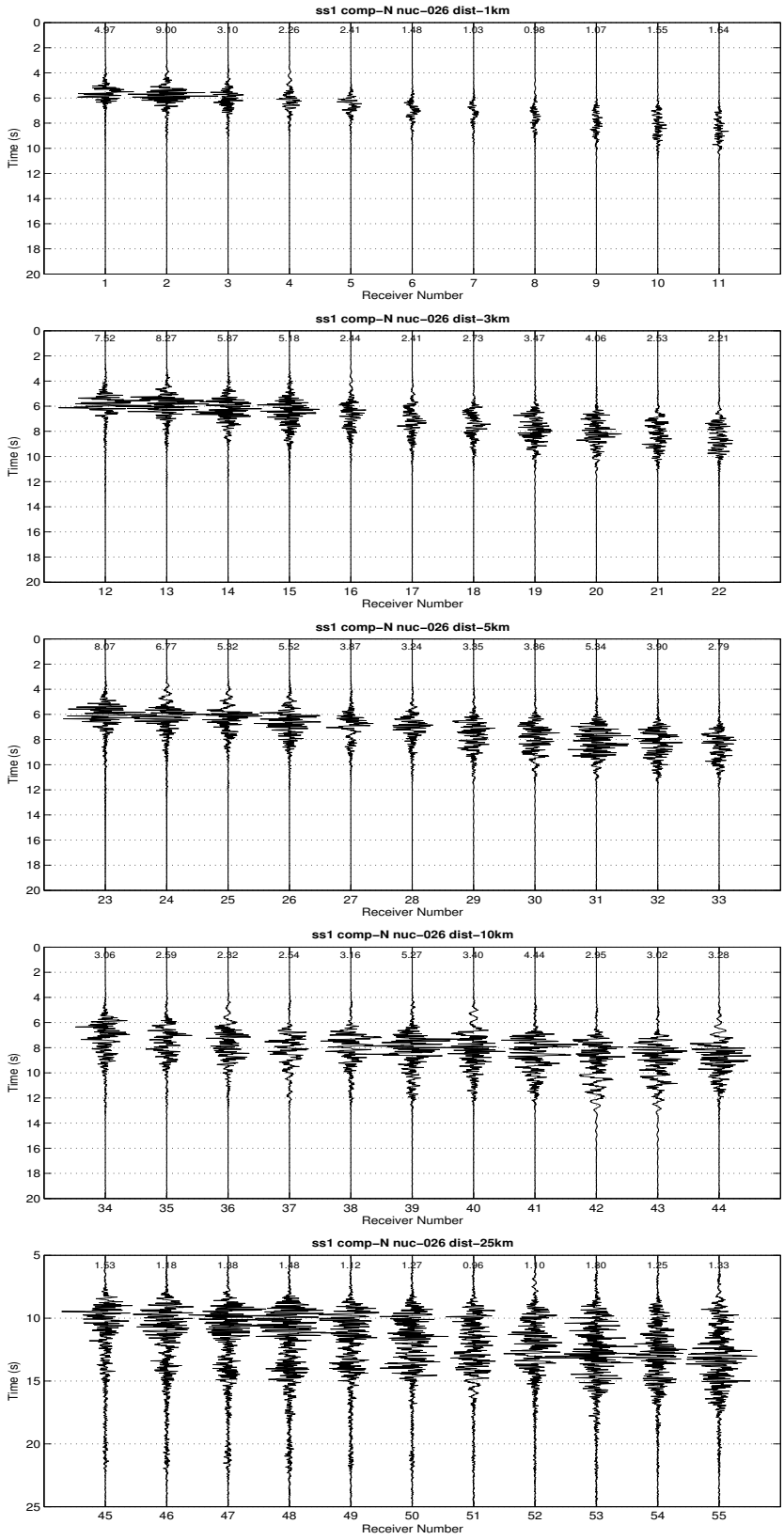

Figure 9: Case SS. Acceleration seismograms computed for slip distribution n. 1 and unilateral rupture propagation toward North (nucleation point 26 in Figure 4). Horizontal North component. The values on the top of the traces indicate the maximum acceleration (in m/s^2).

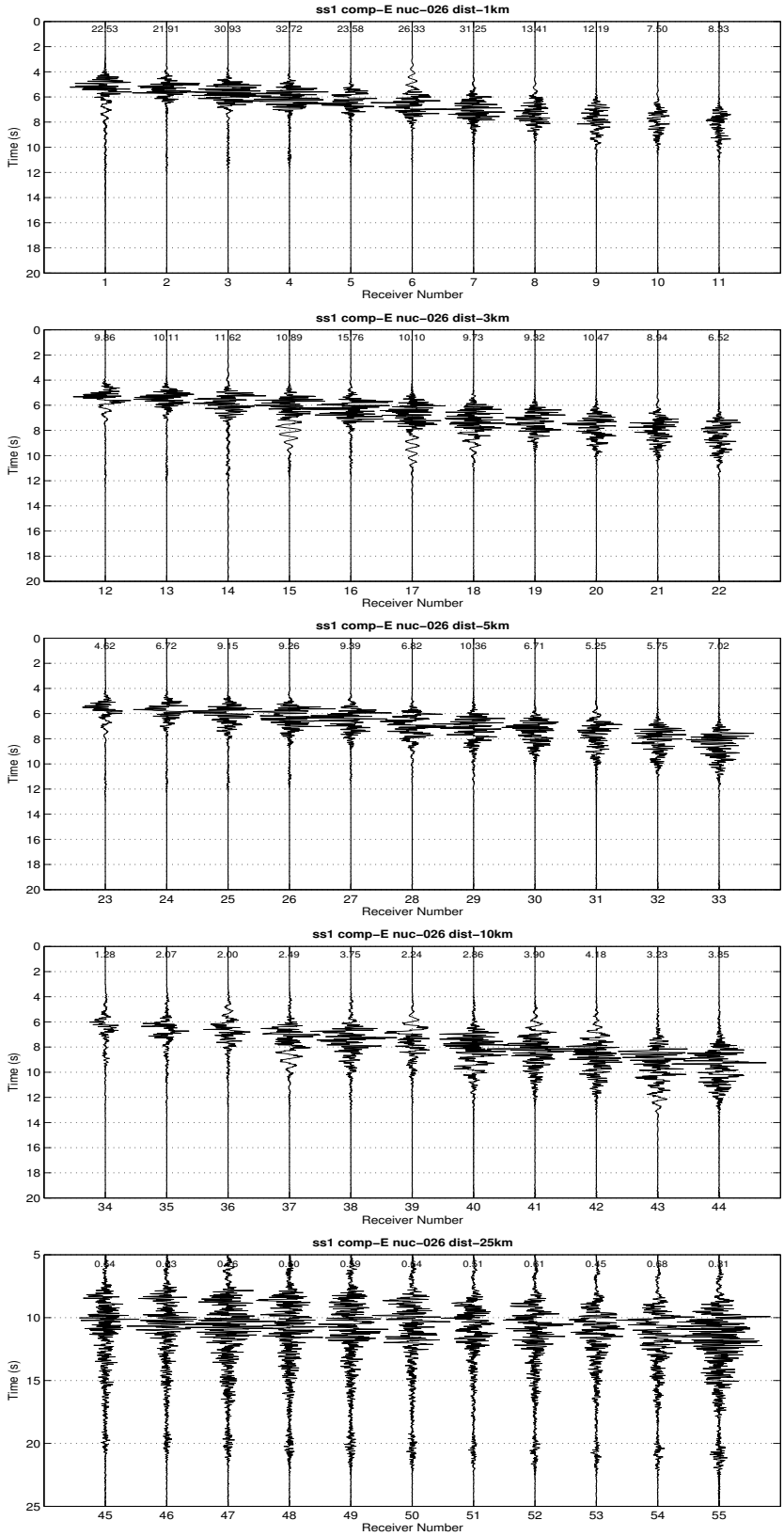

Figure 10: Same as Figure 9, but East component.

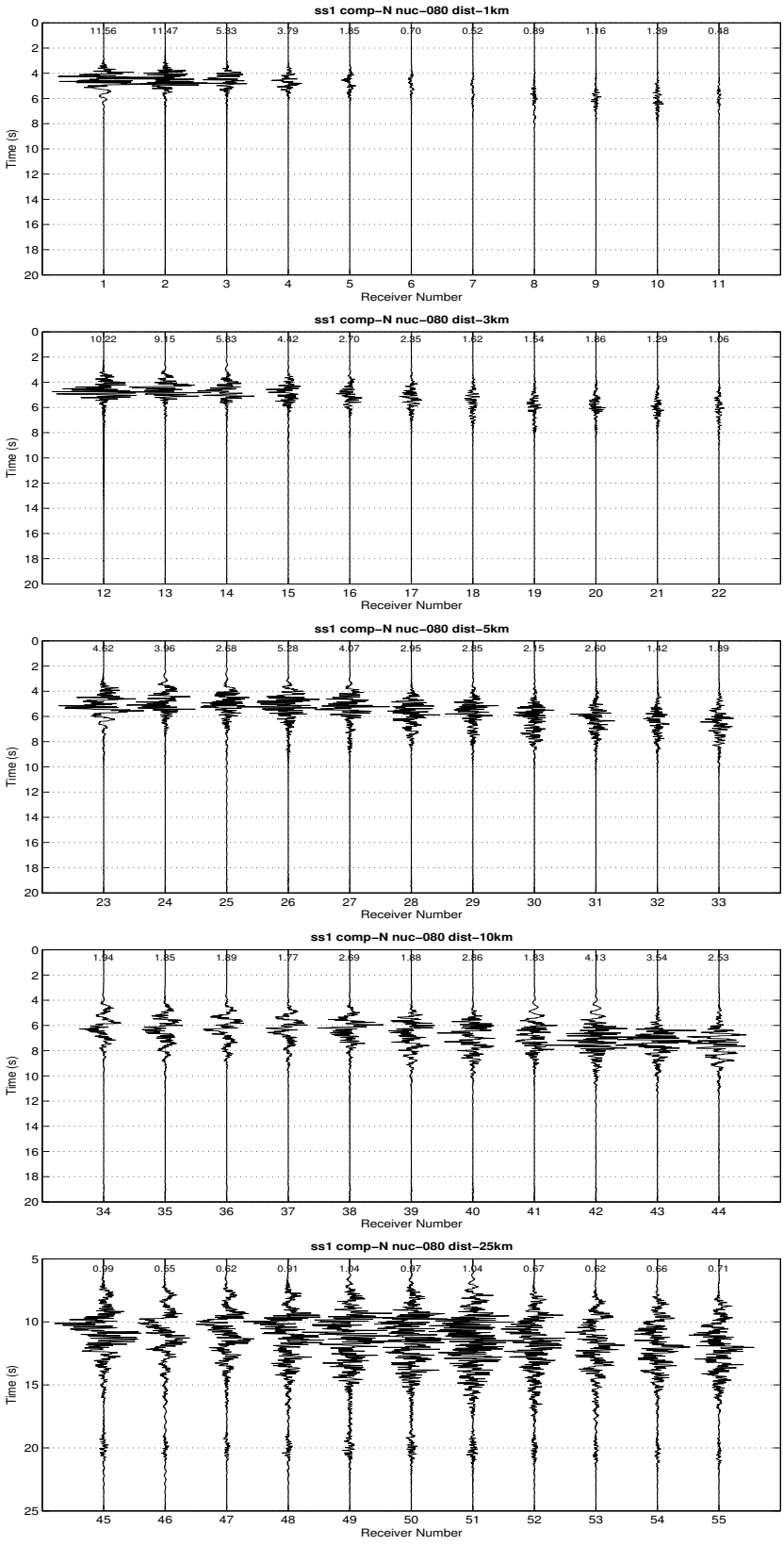

Figure 11: Same as Figure 9, but for bilateral rupture propagation (nucleation point n. 80). Horizontal North component.

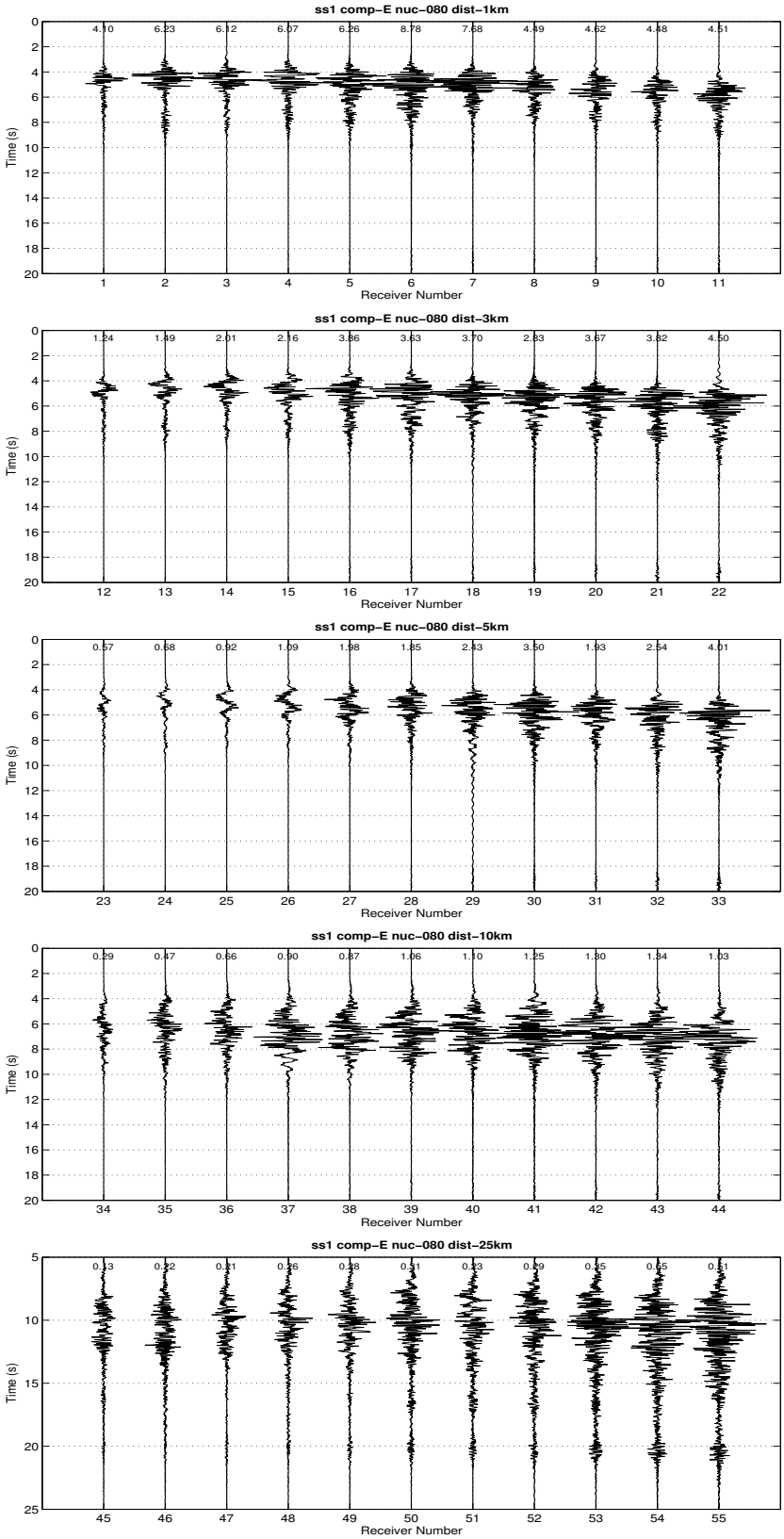

Figure 12: Same as Figure 11, but East component.

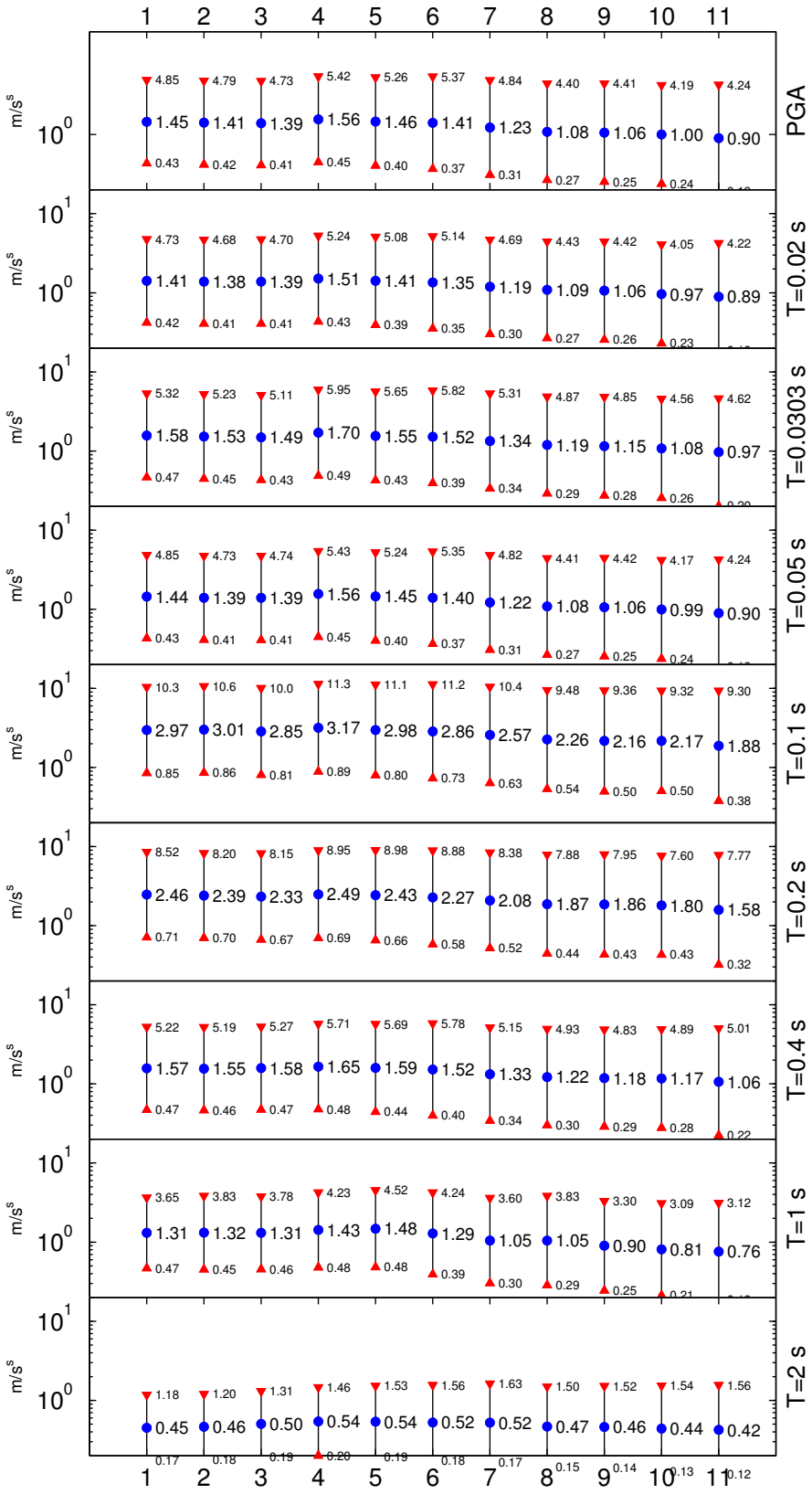

Figure 13: Case SS. Peak ground acceleration and spectral accelerations at distance 1 km. Blue bullet: mean value of the two horizontal components. Red triangles: mean value plus/minus the first standard deviation. Values are in in m/s^2.

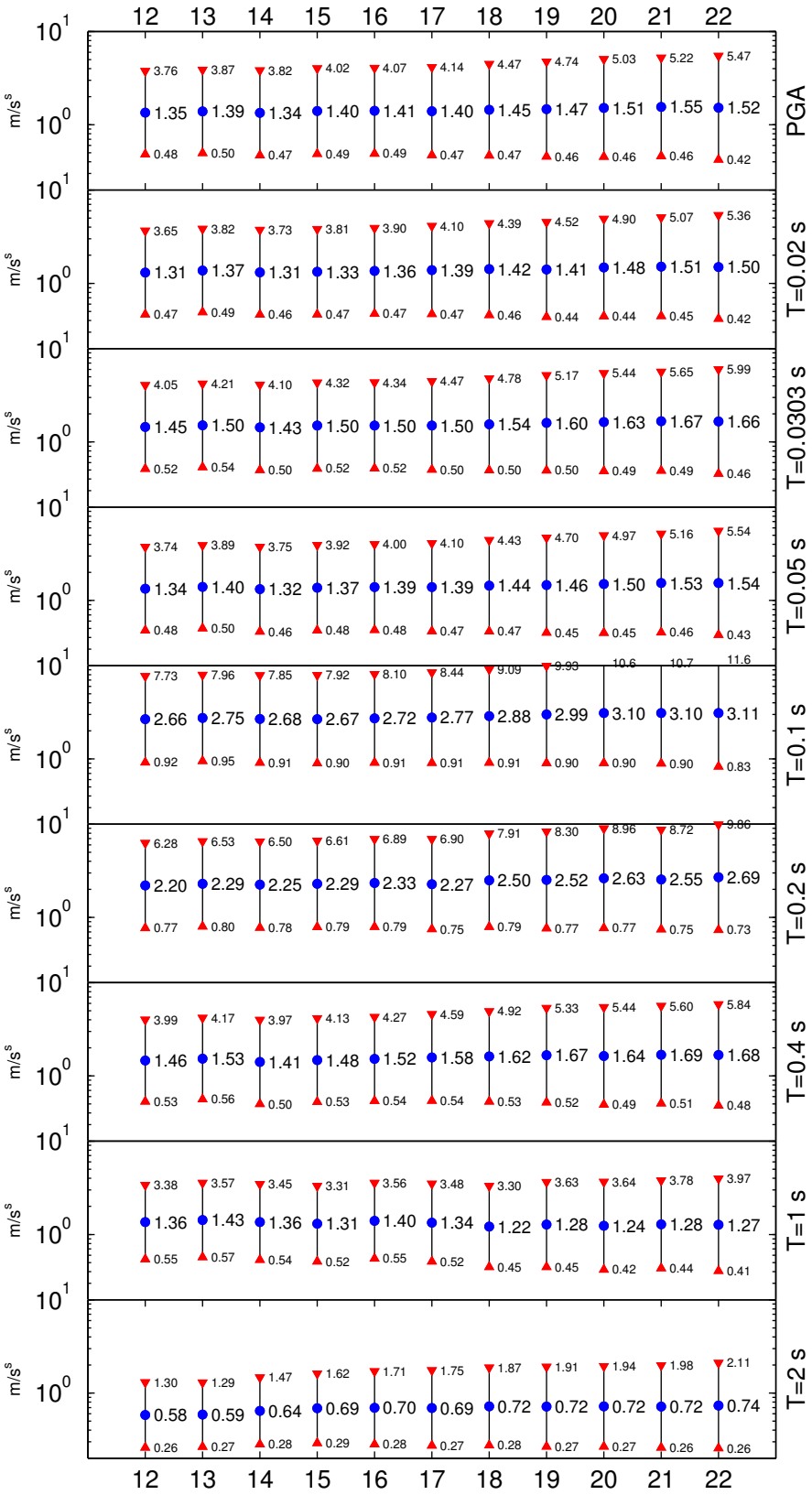

Figure 14: Same as Figure 13, but for distance 3 km.

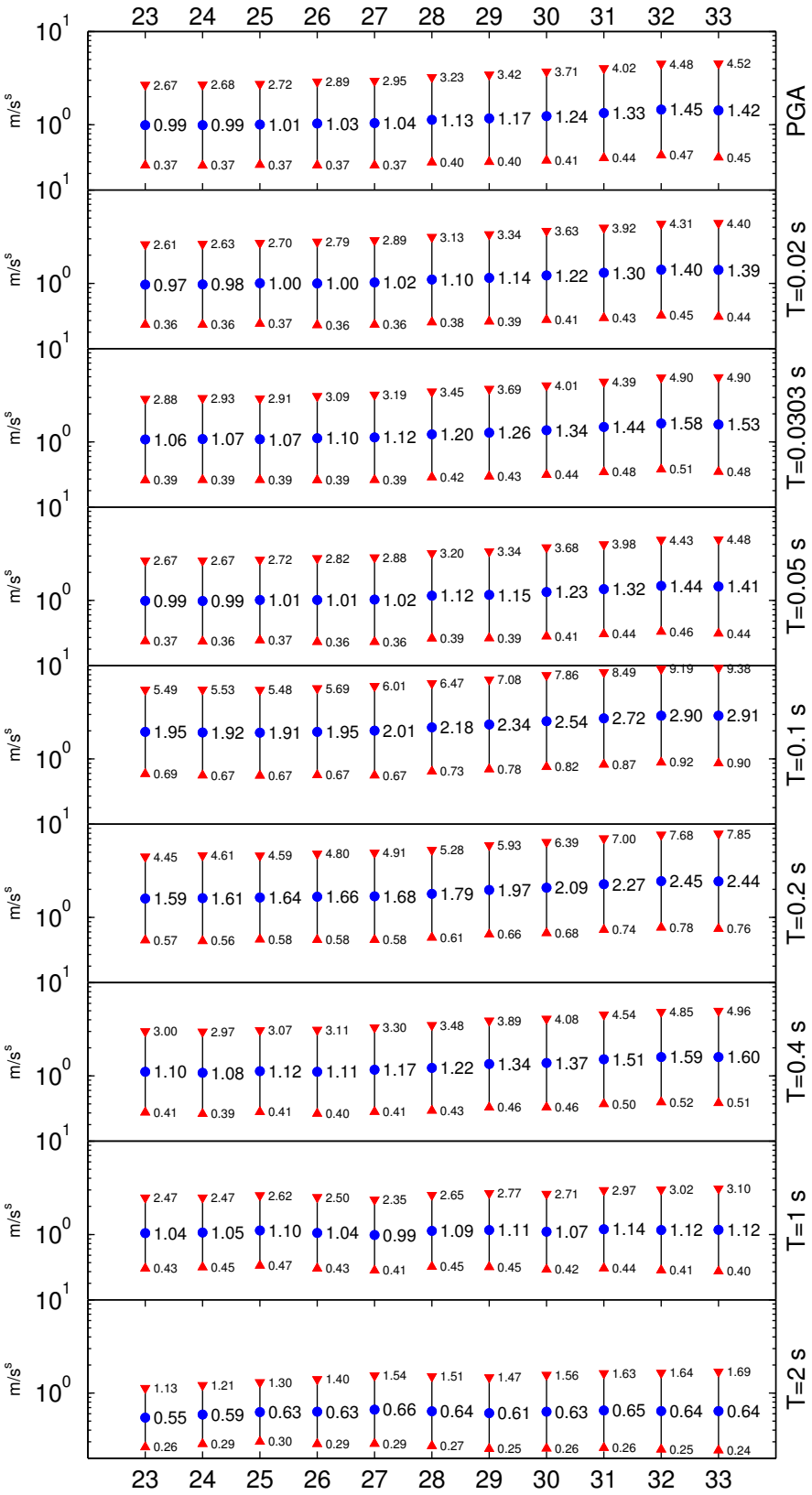

Figure 15: Same as Figure 13, but for distance 5 km.

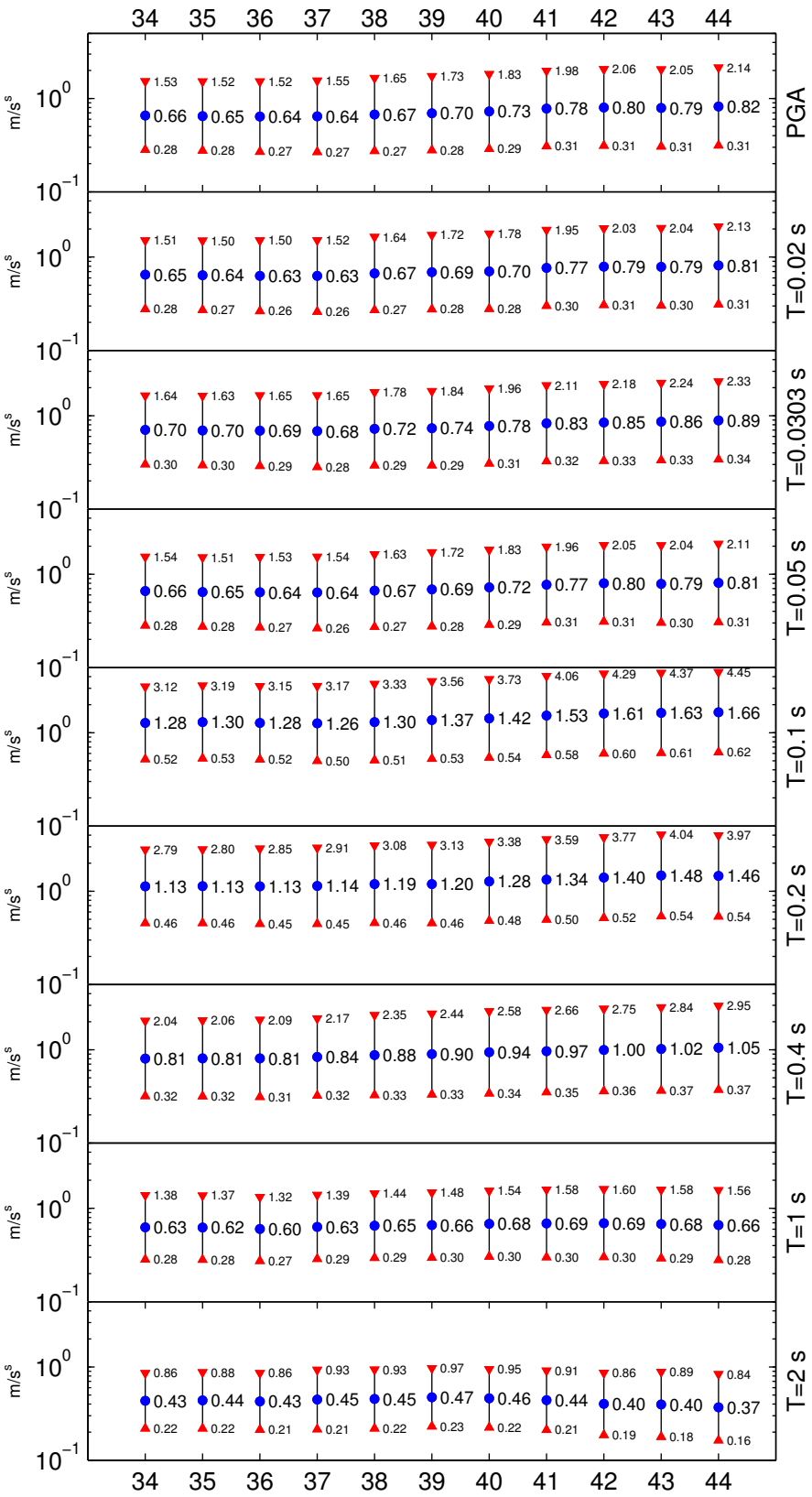

Figure 16: Same as Figure 13, but for distance 10 km.

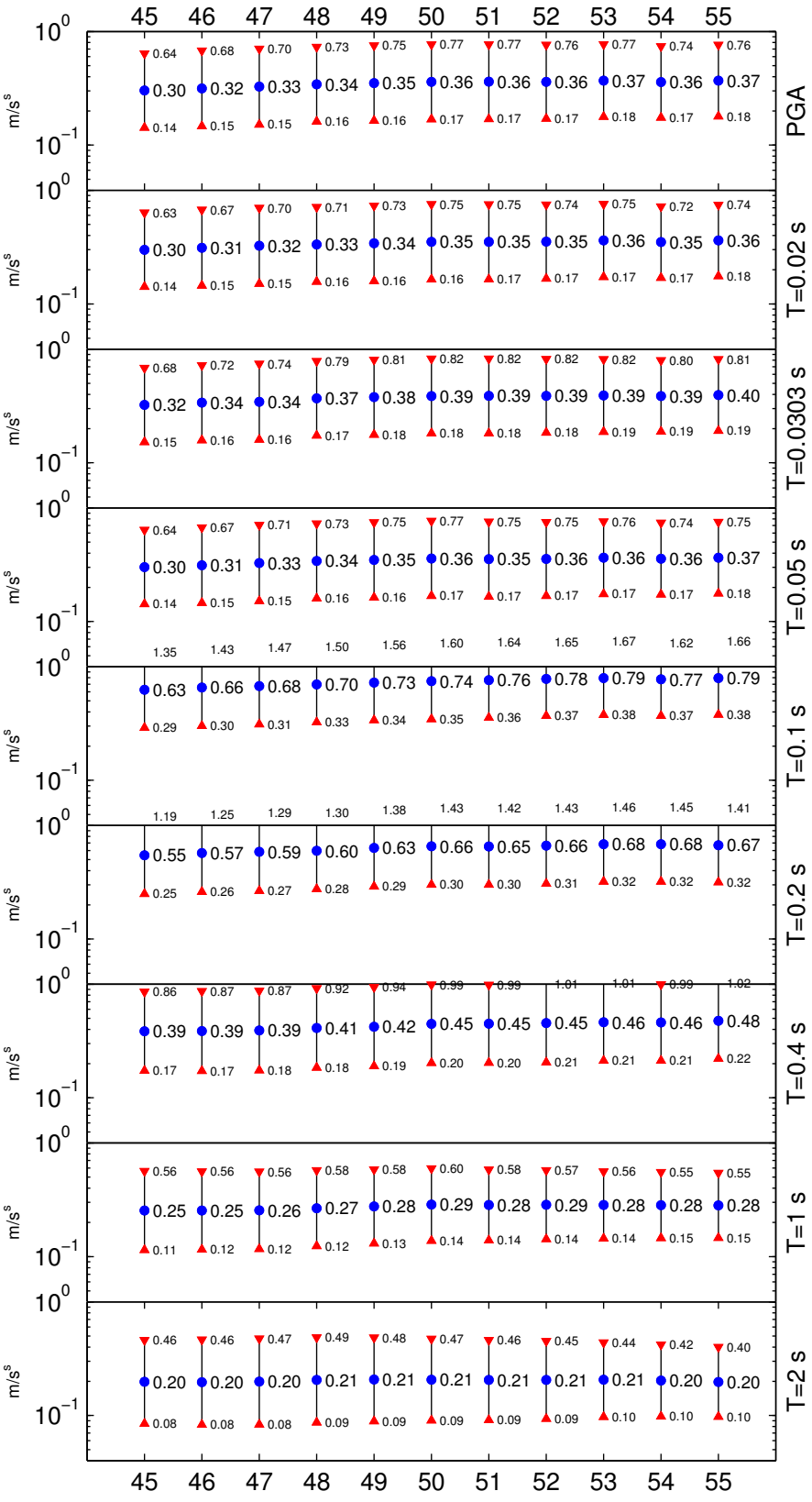

Figure 17: Same as Figure 13, but for distance 25 km.

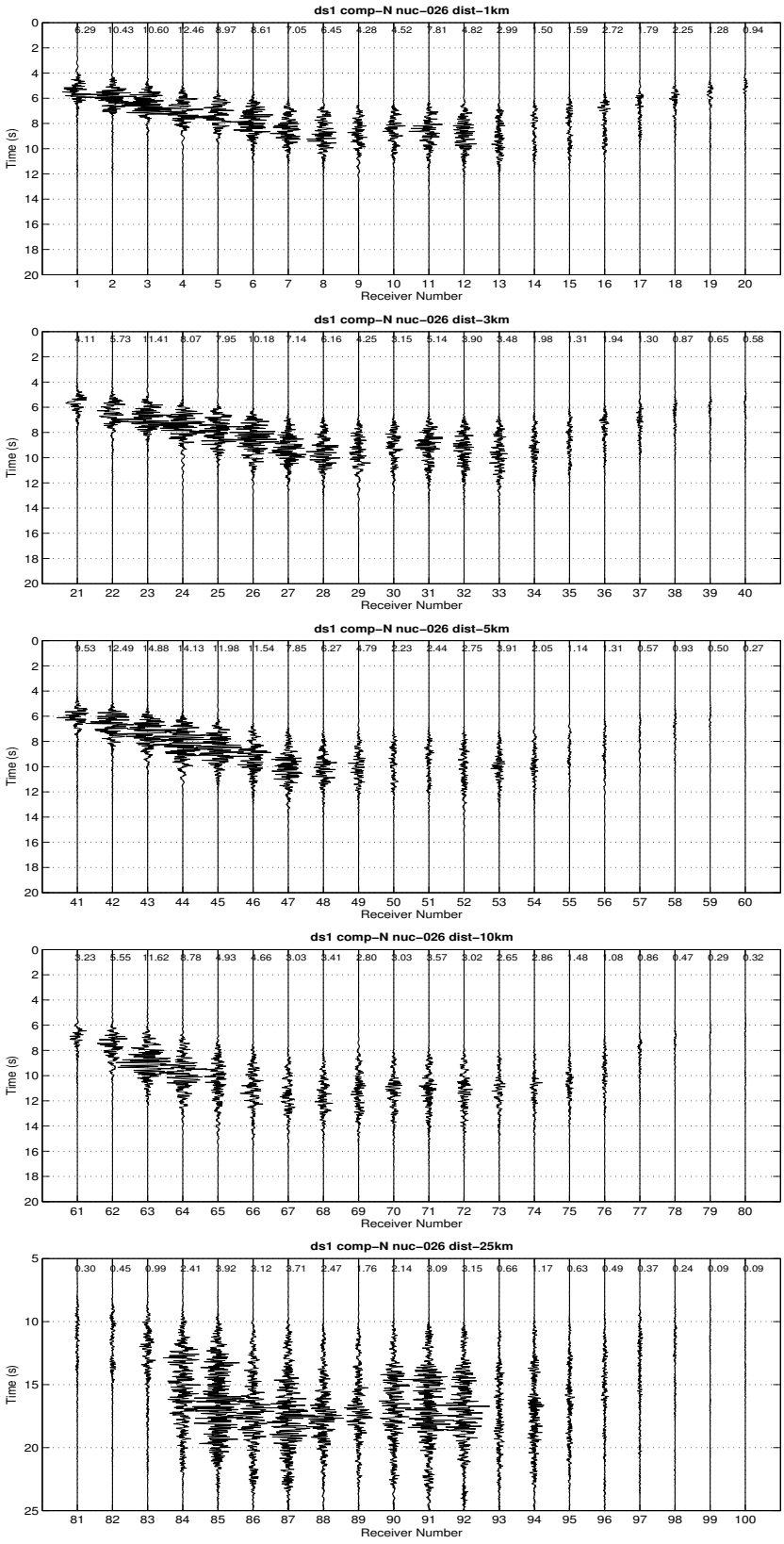

Figure 18: Case DS. Acceleration seismograms computed for slip distribution n. 1 and unilateral rupture propagation toward North (nucleation point 26). Horizontal North component. The numbers indicate the maximum acceleration (in m/s^2).

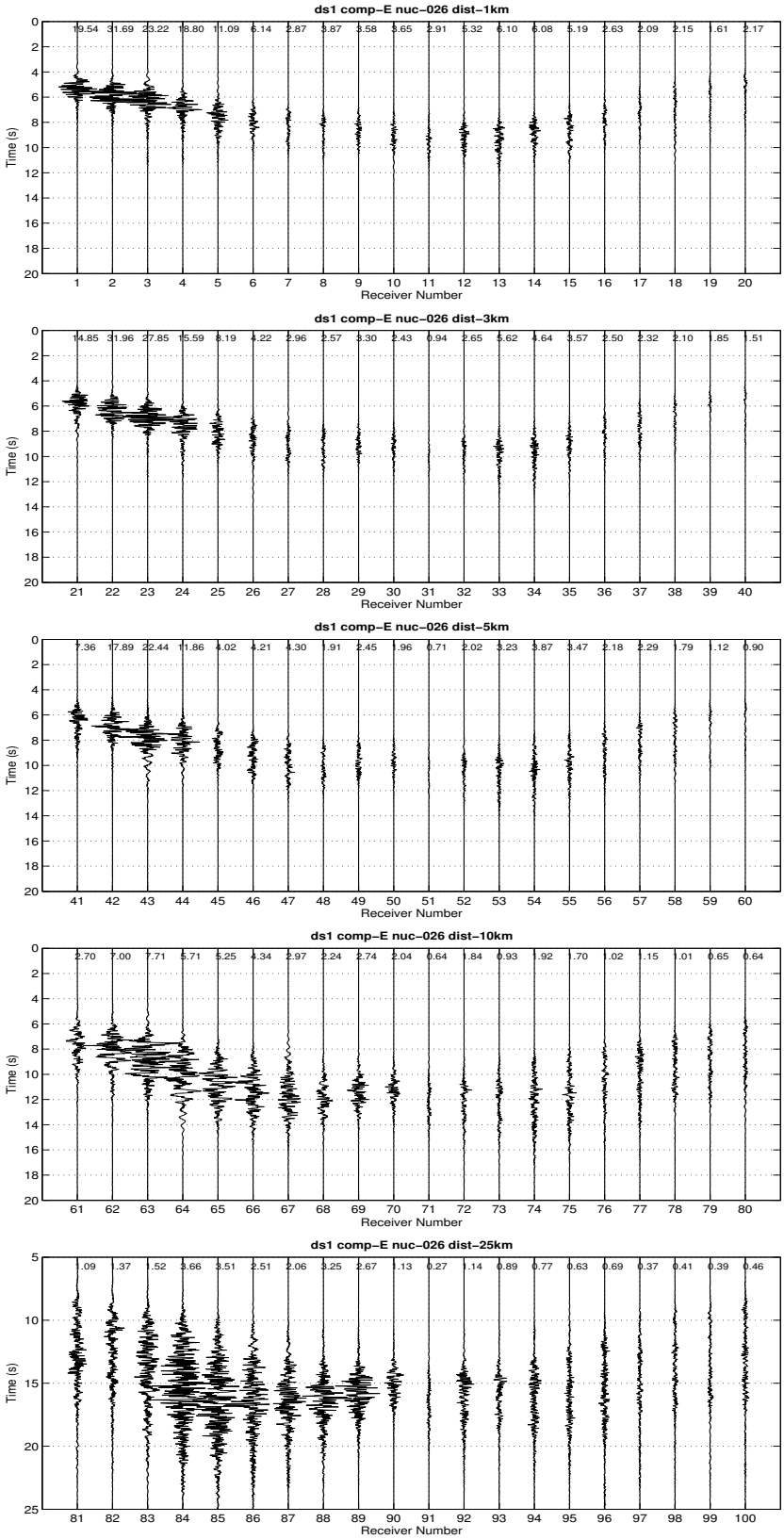

Figure 19: Same as Figure 18, but East component.

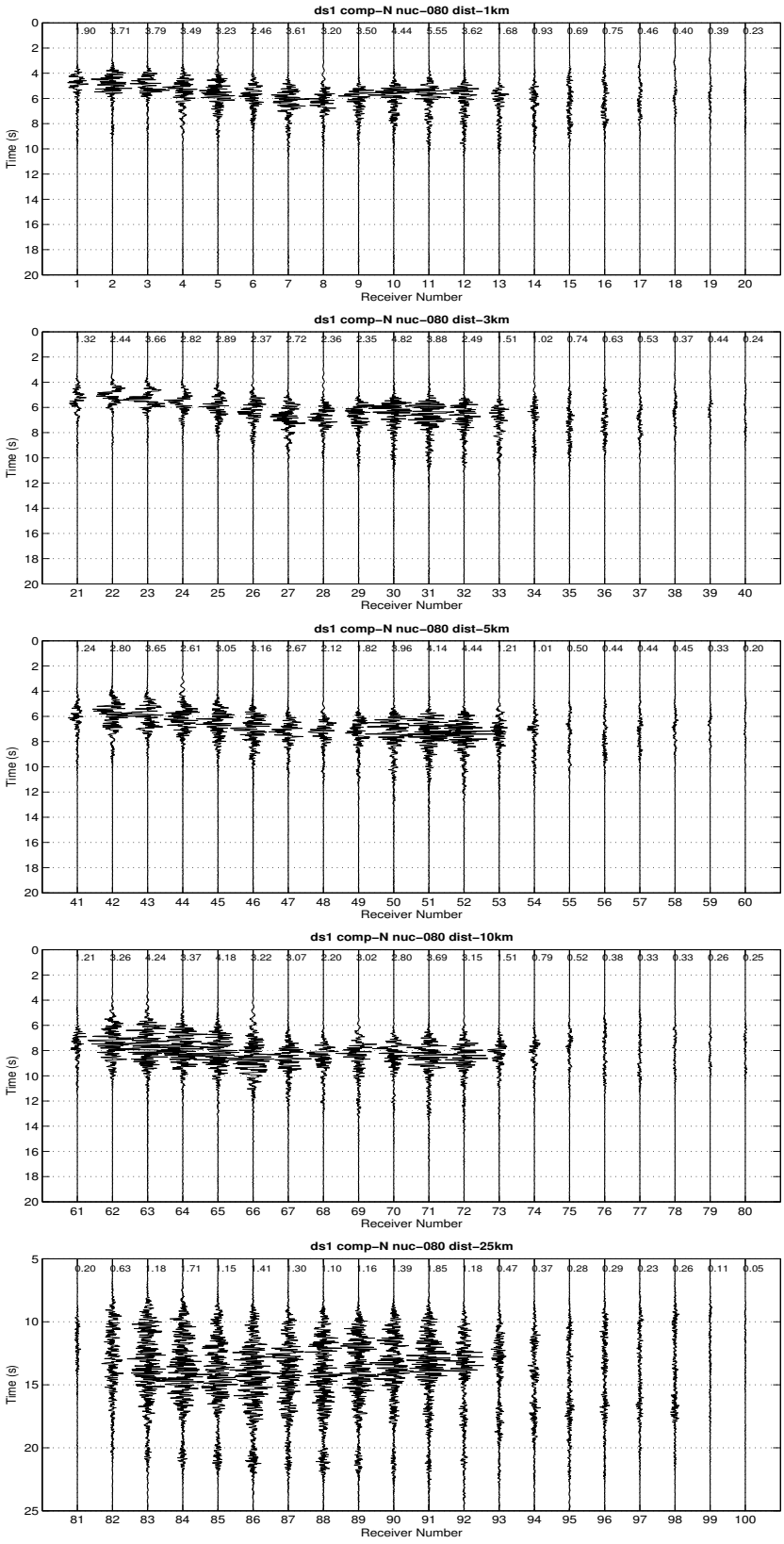

Figure 20: Same as Figure 18, but for bilateral rupture propagation (nucleation point n. 80). Horizontal North component.

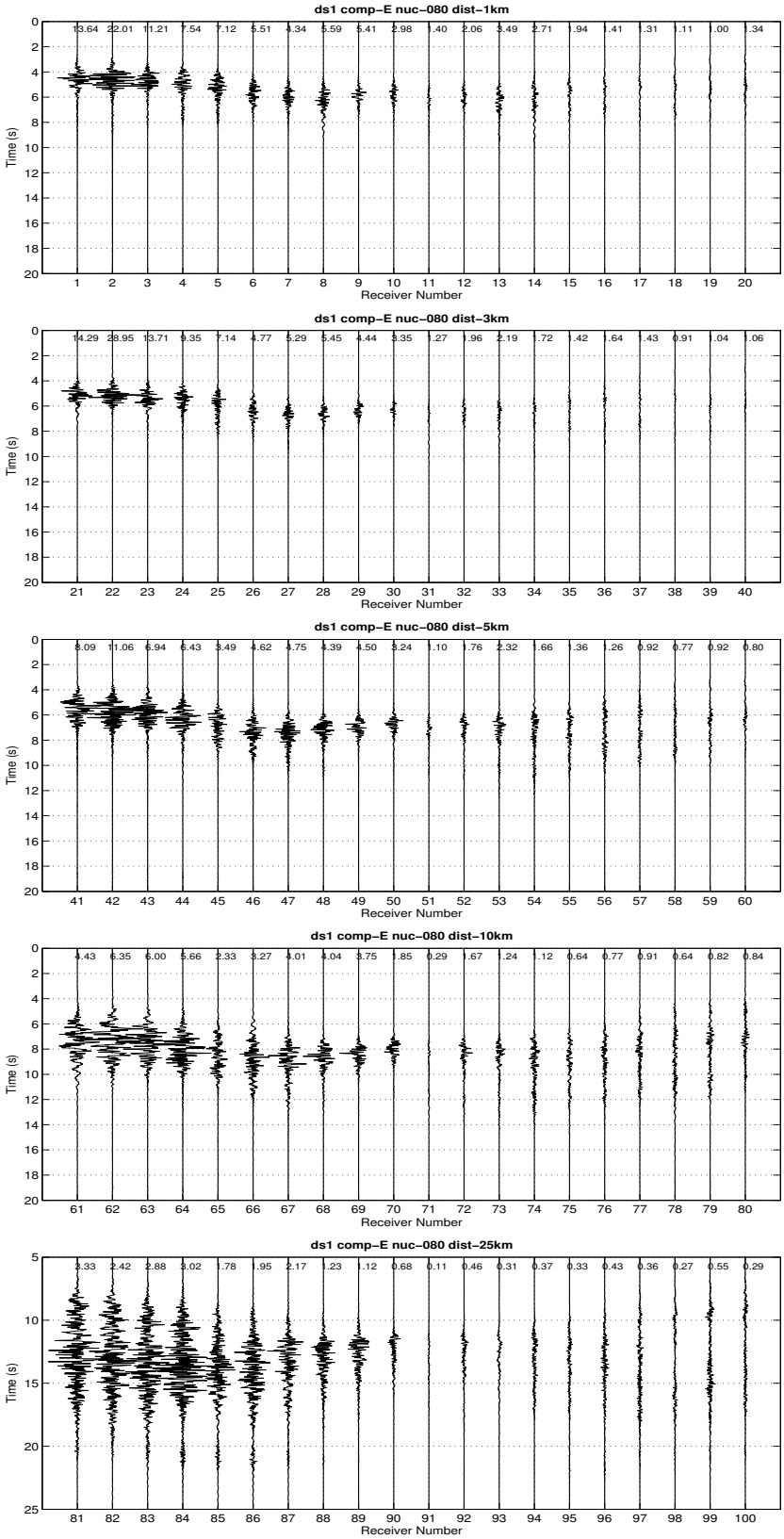

Figure 21: Same as Figure 20, but East component.

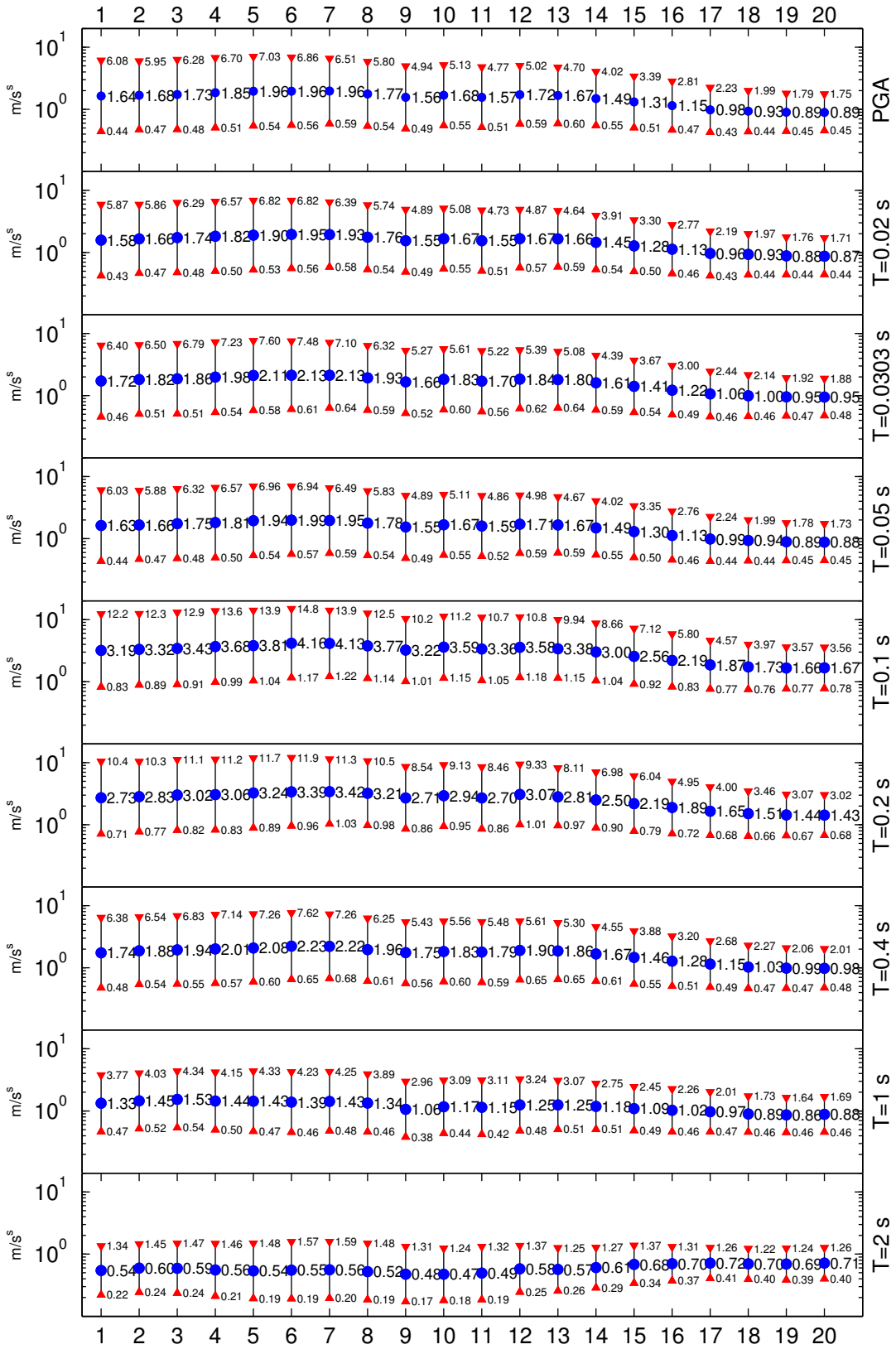

Figure 22: Case DS. Peak ground acceleration and spectral accelerations at distance 1 km. Blue bullet: mean value of the two horizontal components. Red triangles: mean value plus/minus the first standard deviation. Values are in in m/s^2.

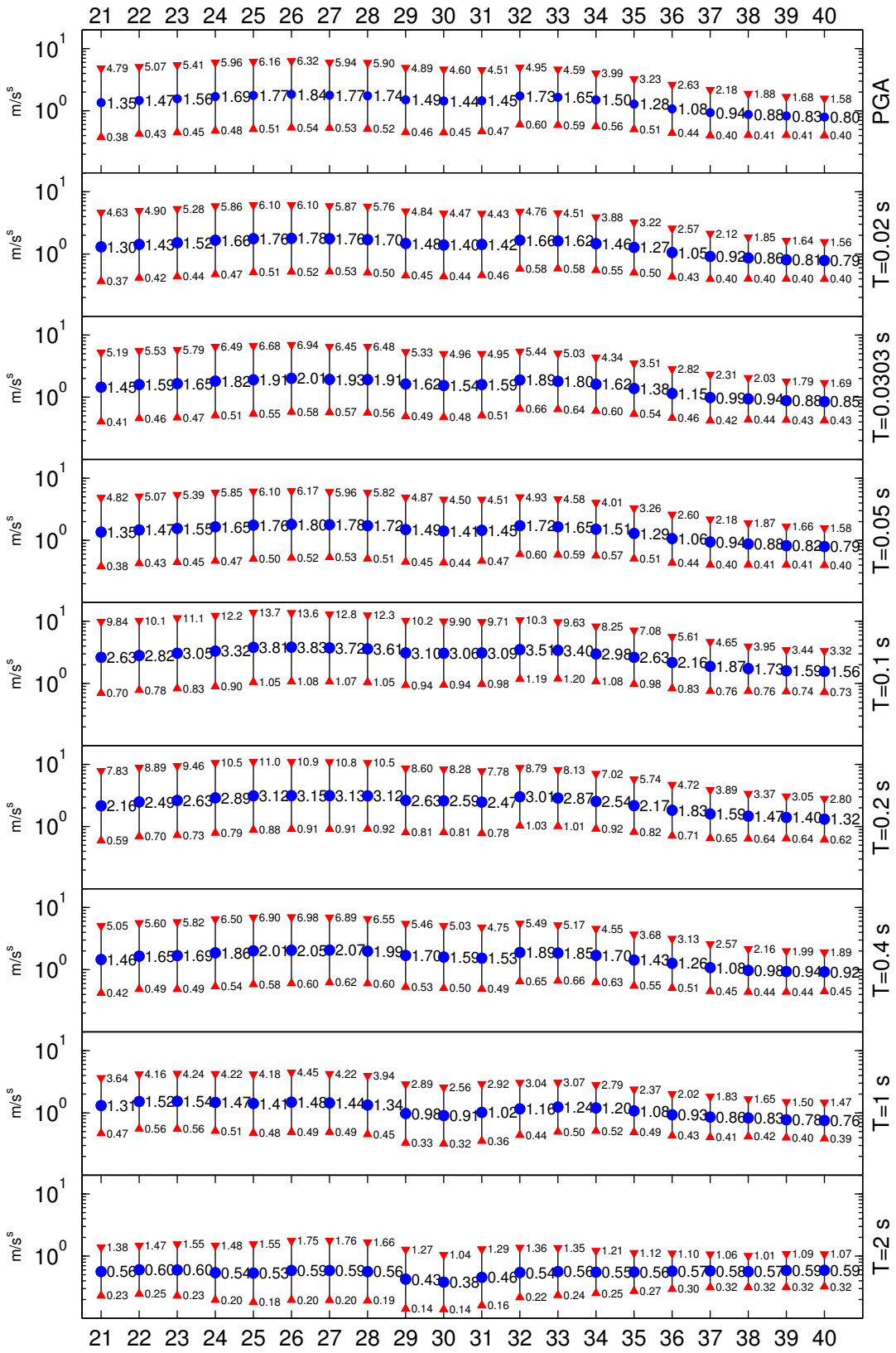

Figure 23: Same as Figure 22, but for distance 3 km.

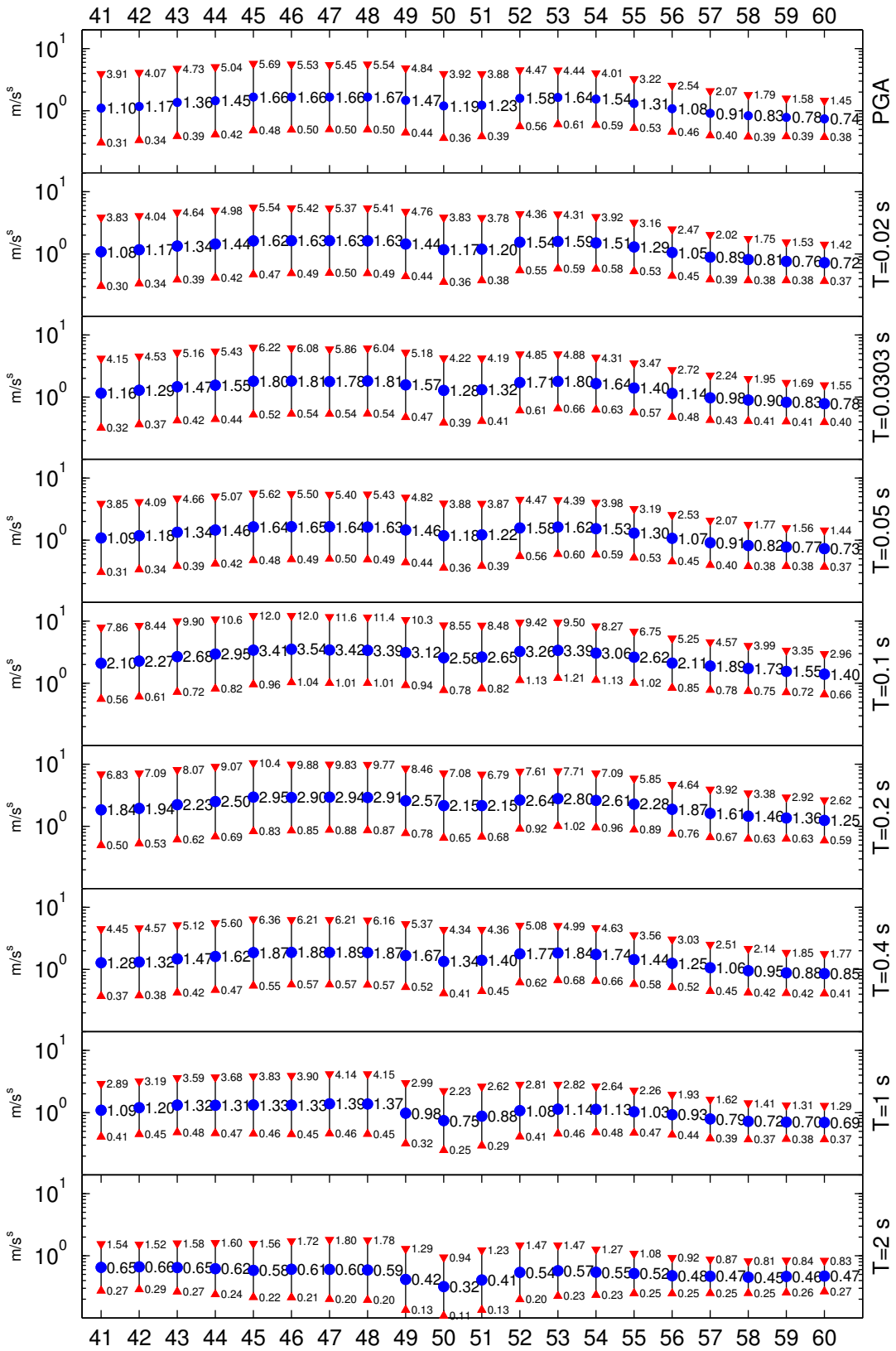

Figure 24: Same as Figure 22, but for distance 5 km.

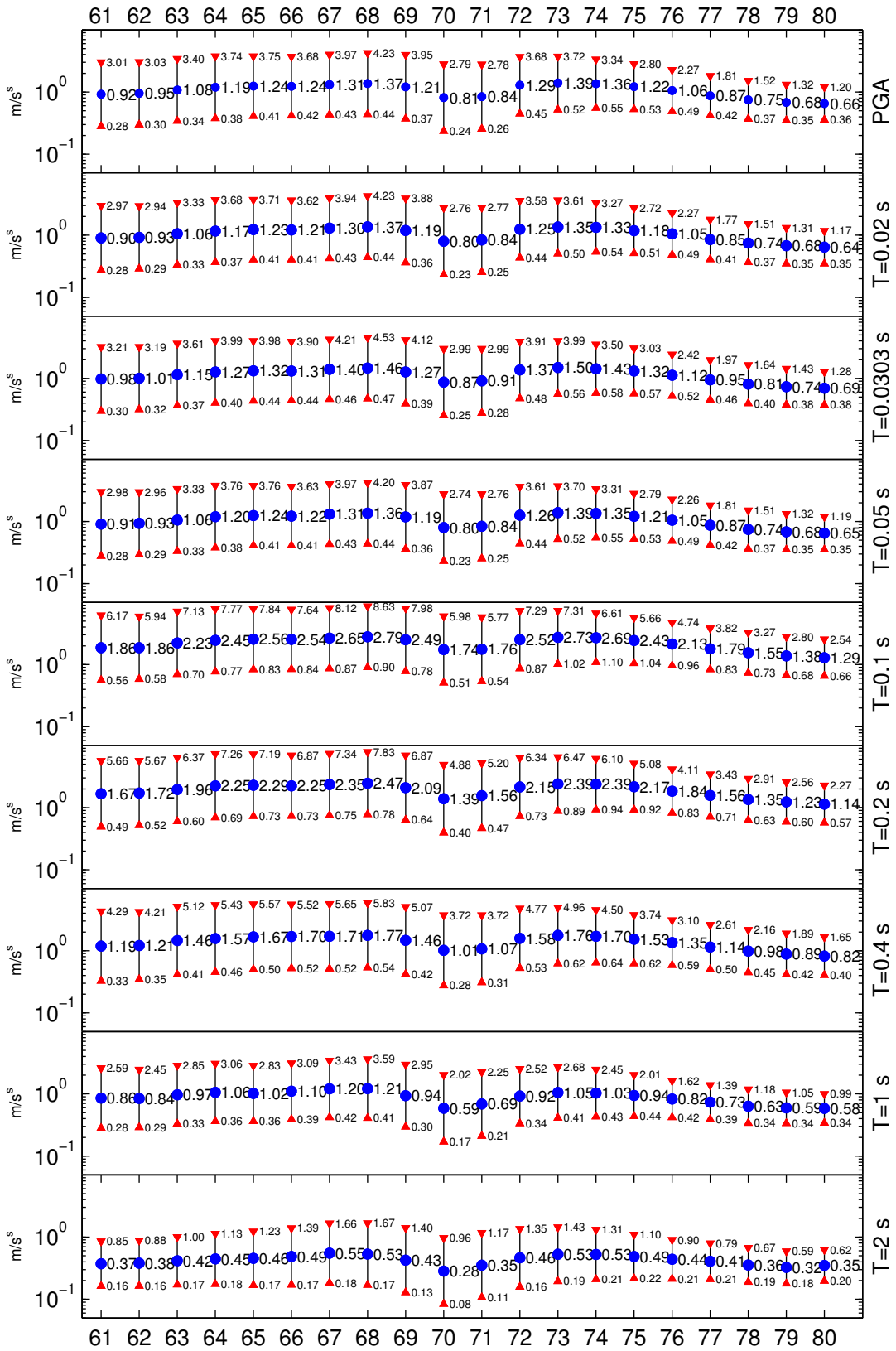

Figure 25: Same as Figure 22, but for distance 10 km.

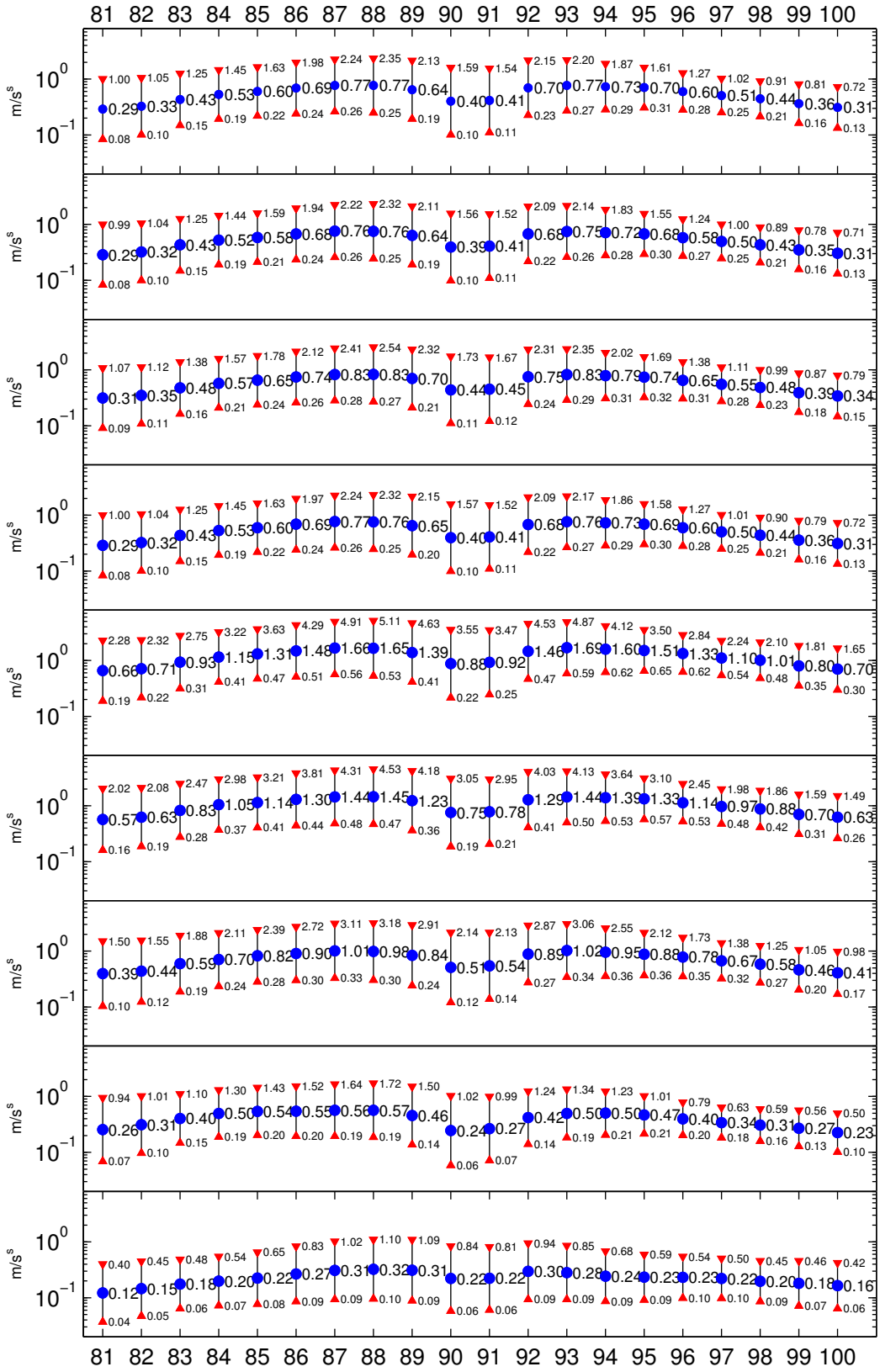

Figure 26: Same as Figure 22, but for distance 25 km.